Fortschritt-Berichte VDI

VDI

Reihe 17

Biotechnik/
Medizintechnik

Dipl.-Min. Berit Müller,
Bad Säckingen

Nr. 294

# Near-net-shape fabrication of open-porous bone replacement materials of calcium phosphate and protein

# ENDKONTURNAHE HERSTELLUNG EINES OFFENPORIGEN KNOCHENERSATZMATERIALS AUS CALCIUMPHOSPHAT UND PROTEINEN

---

# NEAR-NET-SHAPE FABRICATION OF OPEN-POROUS BONE REPLACEMENT MATERIALS OF CALCIUM PHOSPHATE AND PROTEIN

Dem Fachbereich Produktionstechnik

der

Universität Bremen

zur Erlangung des Grades

Doktor-Ingenieur

genehmigte

**Dissertation**

von

Dipl.-Min. Berit Müller

Gutachter: Prof. Dr.-Ing. Kurosch Rezwan

Prof. Dr.-Ing. Lucio Colombi Ciacchi

Tag der mündlichen Prüfung: 27.04.2017

Fortschritt-Berichte VDI

Reihe 17

Biotechnik/
Medizintechnik

Dipl.-Min. Berit Müller,
Bad Säckingen

Nr. 294

# Near-net-shape fabrication of open-porous bone replacement materials of calcium phosphate and protein

Müller, Berit
**Near-net-shape fabrication of open-porous bone replacement materials of calcium phosphate and protein**
Fortschr.-Ber. VDI Reihe 17 Nr. 294. Düsseldorf: VDI Verlag 2017.
104 Seiten, 35 Bilder, 4 Tabellen.
ISBN 978-3-18-329417-6, ISSN 0178-9600,
€ 43,00/VDI-Mitgliederpreis € 38,70.

**Für die Dokumentation:** Biocompatibility – Bioresorbability – Bone Replacement – Calcium Phosphate – Freeze Gelation – Local Drug Release – Lysozyme – Serum Albumin – Zeta Potential

As today's synthetic bone implants fulfil the requirements for the repair of bone defects only in part continuous research for their improvement is ongoing. This work aims at the fabrication of bone replacement materials with bone-like properties regarding composition, structure, mechanical stability, and resorbability. As appropriate fabrication method, the slurry-based freeze gelation process was chosen. It allows the direct incorporation of active bio-relevant compounds, such as proteins, during scaffold processing. Moreover, the process enables the fabrication of complex-shaped and open-porous scaffolds. As principal components for the scaffolds calcium phosphate and protein were selected as they are biocompatible and resorbable. This work analyses the interaction between calcium phosphate and protein in suspension and investigates the suitability of the fabricated calcium phosphate/protein scaffolds as bone replacement material and drug release depot.

**Bibliographische Information der Deutschen Bibliothek**
Die Deutsche Bibliothek verzeichnet diese Publikation in der Deutschen Nationalbibliographie; detaillierte bibliographische Daten sind im Internet unter http://dnb.ddb.de abrufbar.

**Bibliographic information published by the Deutsche Bibliothek**
(German National Library)
The Deutsche Bibliothek lists this publication in the Deutsche Nationalbibliographie (German National Bibliography); detailed bibliographic data is available via Internet at http://dnb.ddb.de.

Dissertation Universität Bremen



Als Manuskript gedruckt. Printed in Germany.
ISSN 0178-9600
ISBN 978-3-18-329417-6

## Acknowledgement

I would like to thank Prof. Dr.-Ing. Kurosch Rezwan for the opportunity of developing this work and his support and overall his patience during the long process of finishing this work accompanying to my job.
I want to thank Prof. Dr.-Ing. Lucio Colombi Ciacchi for agreeing to be my co-examiner. Many thanks go to Dr. Laura Treccani for co-advising and supporting me in my work and above all for her friendship.
I would like to thank all my colleagues during my time in Bremen for the good working atmosphere and all their help. I especially thank Cristian Nuortila, Christian Ellenberg and Tina Kühn for their support in lab-related problems.
I would like to thank Dr. Armin Kirsten for proof-reading part of this work.
I am grateful to all my friends and family who constantly motivated me to finish this work.
I want to thank Michael Gödiker for proof-reading part of this work, his support and patience in the last months, and for calming me down in stressful moments.
I thank my father Uwe Müller for his support during my whole career.
I want to dedicate this work to my late mother Bettina Müller who always encouraged me in my scientific work.

# Table of Contents

## *Summary*

As today's synthetic bone implants fulfil the requirements for the repair of bone defects only in part, this work aims at the fabrication of bone replacement materials with bone-like properties regarding composition, structure, mechanical stability, and resorbability. As appropriate fabrication method, the slurry-based freeze gelation process was chosen. It allows the direct incorporation of active bio-relevant compounds, such as proteins, during scaffold processing. The process, moreover, enables the fabrication of complex-shaped and open-porous scaffolds. As they are biocompatible and resorbable calcium phosphate and protein were selected as principal components for the scaffolds.

In the first part of this work the interaction of calcium phosphate and protein in suspension was investigated by combining zeta potential and VIS spectroscopy measurements. Two at neutral pH oppositely charged model proteins, bovine serum albumin with an acidic and lysozyme with an alkaline isoelectric point, were employed to investigate the protein adsorption behaviour of hydroxyapatite and β-tricalcium phosphate, the most relevant calcium phosphates for the fabrication of bone implants. Both calcium phosphate powders could bind sufficient amounts of acidic and alkaline protein.

Based on this knowledge calcium phosphate/protein scaffolds were fabricated by freeze gelation process and their suitability as bone replacement material investigated by different methods. It is shown that the hydroxyapatite/protein composites feature porosities from 50% to 70% and a mechanical strength ranging from 2 to 6 MPa comparable to that of human spongious bone. Scaffold biocompatibility and resorption behaviour were assessed by *in vivo* tests with adult domestic pigs. After implantation, composites were resorbed up to 50 % after only 4 weeks and up to 65 % after 8 weeks. In addition, 14 % new bone formation after 4 weeks and 37 % after 8 weeks were detected.

Finally, to verify that the processing does not impair biomolecule activity, the antibacterial effectiveness of hydroxyapatite/lysozyme scaffolds was tested. Therefore different amounts of lysozyme from 0.5 to 2.5 wt.% were incorporated into HAp scaffolds. A complete dieback of *M. luteus* bacteria when in contact with the scaffolds was observed, higher lysozyme content leading to faster dieback. The lysozyme

release from the scaffolds by degrees over a time period of at least 9 days proofs the scaffolds attractiveness as depot for localised drug delivery of antibacterial-effective and bone-growth-enhancing drugs.

## *Zusammenfassung*

Da heutige synthetische Knochenimplantate die Anforderungen für die Heilung von Knochendefekten nur teilweise erfüllen, ist das Ziel dieser Arbeit, Knochenersatzmaterialien mit knochenähnlichen Eigenschaften, in Bezug auf Materialzusammensetzung, Aufbau, Festigkeit und Resorbierbarkeit, herzustellen. Als geeignete Herstellungsmethode wurde das Gefriergelieren ausgewählt, ein auf Schlickertechnik basierender Prozess. Beim Gefriergelierprozess können aktive Biomoleküle, wie zum Beispiel Proteine, in das Keramikgerüst eingelagert werden. Darüber hinaus ermöglicht der Prozess die endkonturnahe Herstellung komplex geformter und offenporöser Komposite. Wegen ihrer Biokompatibilität und Resorbierbarkeit wurden Calciumphosphate und Proteine als Hauptbestandteile für die Komposite ausgewählt.

Im ersten Teil dieser Arbeit wurden die Wechselwirkungen von Calciumphosphat und Proteinen in Suspension mit Zetapotential- und VIS-Spektrometriemessungen untersucht. Dafür wurden zwei bei pH 7 entgegengesetzt geladene Modell-Proteine, bovines Serumalbumin mit isoelektrischem Punkt im Sauren und Lysozym mit isoelektrischem Punkt im Basischen, und zwei Calciumphosphate, Hydroxyapatit und β-Tricalciumphosphat, die größte Bedeutung für die Herstellung von Knochenimplantaten haben, ausgewählt. Beide Calciumphosphatpulver konnten in ausreichendem Maße saures und alkalines Protein binden.

Basierend auf diesen Voruntersuchungen wurden Calciumphosphat/Protein-Komposite mittels Gefriergelierprozess hergestellt und ihre Eignung für die Anwendung als Knochenersatzmaterial geprüft. Es zeigte sich, dass die Komposite mit ihrer Porosität von 50% bis 70% und ihrer Biegefestigkeit von 2 bis 6 MPa vergleichbar mit humaner *Spongiosa* sind. Die Biokompatibilität und Degradierbarkeit wurde durch

*in vivo* Untersuchungen mit Hausschweinen getestet. Nach Implementierung wurden die Komposite bis zu 50 % nach 4 Wochen und bis zu 65 % nach 8 Wochen resorbiert. Zusätzlich konnte im Wundbereich nach 4 Wochen bis zu 14 % und nach 8 Wochen bis zu 37 % neue Knochenbildung nachgewiesen werden.

Abschließend wurden die antibakteriellen Eigenschaften von Hydroxyapatit/Lysozym-Kompositen geprüft, um sicherstellen zu können, dass der Gefriergelierprozess die Biomolekül-Aktivität nicht beeinträchtigt. Dafür wurden Komposite mit 0,5 bis 2,5 Gew.% Lysozym hergestellt und in Kontakt mit Bakterien gebracht. Bei *M. luteus* Bakterien führte der Kontakt mit den Kompositen zu einem vollständigen Absterben, welches umso schneller von statten ging je höher die Lysozym-Konzentration in den Kompositen war. Da gezeigt werden konnte, dass Lysozym nur allmählich von den Kompositen über einen Zeitraum von bis zu 9 Tagen abgegeben wird, sind die Komposite interessant als Depots für die direkte Abgabe von antibakteriellen und knochenwachstumsanregenden Wirkstoffen im Wundbereich.

# 1 Introduction

## 1.1 Motivation

In recent years the fabrication of bone replacement materials has become a centre of focus as the demands for bone implants increase due to an ageing society. Defects in bone can be caused by traumas and diseases and are traditionally treated by bone transplants either from the patient himself (autografting) or from donors (allografting). However bone transplants bear the health risks of rejection, disease transmission, and donor site morbidity, and their availability is limited. Therefore interested in the development of synthetic bone replacement materials has increased [1-4].

Ideally synthetic bone replacement materials must fulfil the following requirements. Their main function is the support of the defect site by sufficient mechanical stability. Moreover they must be biocompatible and non-toxic. To allow ingrowth of bone cells they should provide an open-porous structure. Finally they should be resorbable and promote new bone formation. Only materials closely resembling bone composition can be remodelled by bone cells. These include calcium phosphates, protein and other biomolecules, and some synthetic polymers (for example polylactide) [5].

To stimulate bone cell growth, regeneration, and remodelling bone replacement materials should be functionalised with relevant bio-molecules [3, 6-8]. To combat infection from surgery the incorporation of antibacterial agents is also desirable [9]. Conventional drug delivery by oral administration and injection cannot ensure sufficient concentration of the drug at the defect site [10-12]. Moreover drugs delivered systemically, distributed throughout the body via the blood circulatory system, may result in systemic toxicity [13, 14]. Therefore local drug delivery at the defect site by incorporation of protein into bone implants is desirable.

There is attention on appropriate fabrication methods to develop bone replacement materials with such properties. First of all the processing must allow the fabrication of open-porous scaffolds. Such methods are for example replica techniques, direct foaming, and freeze casting [15-17]. Secondly the processing route must allow near-net-shape fabrication as bone defect sites are often complex-shaped. Thirdly the biocompatibility of the raw components must not be impaired and toxic

additives must be excluded [18]. For many processing routes sufficient stability is only reached by sintering. However sintering often reduces the biocompatibility of scaffolds as their surface becomes smoother and more hydrophobic by evaporating $OH^-$ which will hinders bone cell cultivation [19]. Furthermore as biomolecules are not thermally stable sintering makes one-pot-processing of calcium phosphate/protein scaffolds impossible [20] and incorporation of active biomolecules can then only be achieved by a subsequent functionalisation step, for example by soaking or grafting [21-24]. As this often leads to a poorly controlled biomolecule release within short time [23], processing without sintering is desirable.

Among all processing methods, the freeze gelation process is considered highly feasible for the generation of ceramic scaffolds [25-29]. The freeze gelation process is based on freeze casting, a slurry-based method where open pore channels are achieved by volume expansion of ice when the casted slurry is frozen. However subsequent freeze drying is necessary as the demolded green body is not stable at room temperature. Thereby the ceramic structure gets brittle necessitating sintering for sufficient mechanical stability [15].

For the advanced freeze gelation process a freeze sensitive silica sol is mixed into the slurry. Silica sol gels irreversibly when frozen rendering freeze drying unnecessary and moreover is improving the green body strength sufficiently to forego sintering [30]. Therefore thermally labile biomolecules can be directly incorporated enabling the fabrication of near-net, complex shaped, open-porous calcium phosphate/protein scaffolds in one-step.

### *1.2 Aims of this thesis*

The aim of this thesis is the fabrication of biocompatible, near-net, complex-shaped calcium phosphate/protein scaffolds with tunable porosity, degradability, and handling stability by freeze gelation process.

As calcium phosphate powders hydroxyapatite (HAp) and β-tricalcium phosphate (β-TCP) were selected as they are most commonly used for the fabrication of calcium phosphate-based biocomposites [31]. To be useful for a variety of applications two at neutral pH oppositely charged model proteins, bovine serum albumin (BSA) and lysozyme (LSZ) were chosen. The structure of both proteins is well known [32-35] and the adsorption of BSA and LSZ on various oxide particle surfaces was already

investigated [36-38]. The chosen model proteins represent proteins with acidic (BSA) and alkaline (LSZ) isoelectric point so that the results can be qualitatively transferred to other biomolecules behaviour in combination with calcium phosphates, for example proteins relevant for bone formation.

A first part of this work is aiming to assess the loading capacity of calcium phosphate powder with protein by adsorption which was investigated by combining zeta potential and UV/VIS measurements [36, 39, 40]. On hydrophilic surfaces electrostatic interactions which can be assessed by zeta potential measurements are one of the main factors for the adsorption of biomolecules on particle surfaces [41-46]. UV/VIS spectroscopy was applied to quantify the amount of adsorbed protein.

The second part of this work focuses on the fabrication and characterisation of hydroxyapatite/protein scaffolds with varying BSA and LSZ content. It is assessed how the added protein influences mechanical stability and porosity of the scaffolds. Moreover biocompatibility and degradation behaviour is investigated in vitro (calcium and protein release) and in vivo in a pig model.

In a third part of this thesis it is investigated if the scaffolds are suitable as drug delivery matrices. For this purpose hydroxyapatite/lysozyme scaffolds were fabricated. Lysozyme is an antibacterial effective enzyme and its activity verifiable by bacterial tests [47]. Thereby it could be surveyed if protein activity is impaired by the freeze gelation process. Moreover the drug release rates which are mainly determined by the scaffold into which the drug is loaded and the applied loading method [48, 49] where calculated.

# 2 Basics

## 2.1 Bone

Bone is a natural nanocomposite material consisting of two interlaced components: anorganic bone mineral and organic collagen type I [50].

The mineral in bone is carbonated hydroxyapatite which is a calcium phosphate mineral phase. Hydroxyapatite is a naturally prevalent hexagonal mineral phase forming tabular or needle-like crystals. In bone it forms nano-sized platelets, 30-50 nm in length, 15-30 nm in width, and 2-10 nm in thickness. The stoichiometric chemical composition of hydroxyapatite is $Ca_5(PO_4)_3(OH)$. However in bone the hydroxyapatite is non-stoichiometric with less calcium which leads to a Ca:P ratio of <1.67. In addition it contains impurities, in particular 4 to 6% carbonate and <1% sodium and magnesium [50-52].

Collagen type I is a fibrillar protein not only occurring in bone but in most connective tissues as skin, ligaments, tendons, cartilage, blood vessels and dentin. As all proteins it consists of amino acids forming ~300 nm long so-called tropocollagen molecules which form fibrils of ~1 µm in length. These fibrils build up the actual collagen fibers of ~10 µm in length (Figure 2-1) [53, 54].

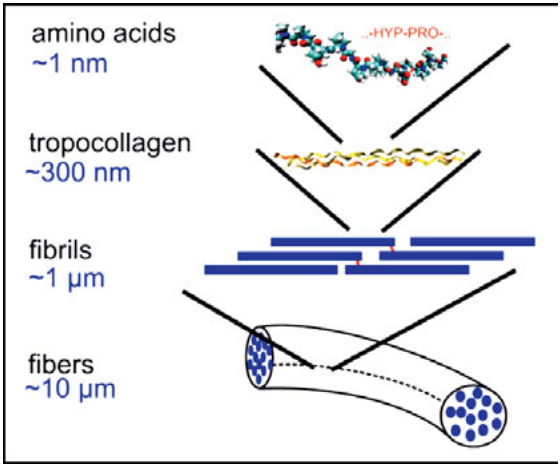


**Figure 2-1. Schematic of the hierarchical structure of collagen (schematic taken from reference [53])**

The bone mineral platelets can be found inside and on the surface of the collagen fibrils. This structure is responsible for the good mechanical properties of bone. Both hydroxyapatite and collagen have only limited mechanical properties. However the unique construction of bone leads to high strength and fracture toughness, as elastic collagen fibers are supported by stiff crystals (Figure 2-2) [55].

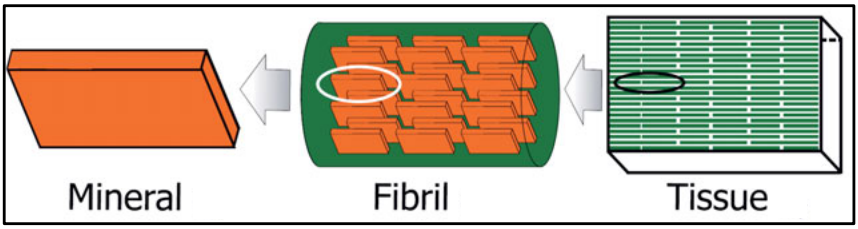


**Figure 2-2. Arrangement of the minerals in bone (schematic taken from reference [55])**

The bone structure is open-porous allowing the networking of bone cells. The bone cells, bone-degrading osteoclasts and bone-forming osteoblasts, are constantly remodelling bone. Thereby in healthy adults all bone is replaced in 3 to 4 years, however this rate is decreasing with age. Bone remodelling allows for constant repair and is essential for the durability of bone [56].

There are two types of bone tissue in the human body: *Compacta* and *Spongiosa*. The *Compacta* is denser and stronger than the *Spongiosa* and forms the outer part of bone whereas the porous *Spongiosa* can be found inside the bone [50].

The Compacta which fulfils the main supporting function has a bending strength of 50 to 150 MPa whereas the Spongiosa with up to 90 % porosity is only 2 to 10 MPa strong [57, 58]. The pore sizes of the *Compacta* range from 1 to 100 µm whereas those of the Spongiosa range from 200 to 400 µm [59].

## *2.2 Bone replacement*

Bone injuries and defects can be caused by traumas, diseases, or aging. To restore normal tissue function of critical-sized defects bone replacement materials are necessary. Ideally such materials resemble the properties of the original tissue as closely as possible, requirements being bone-like composition, structure, and porosity [60]. They also must provide sufficient mechanical stability to sustain bone formation

till completion of bone defect repair. Bone replacement materials should degrade in a controlled manner comparable to native bone tissue and stimulate cell growth and osteoregeneration. Furthermore they should not induce inflammatory responses or contain toxic degradation products [61]. Bone replacement materials can be of natural origin or fabricated synthetically [31].

The properties of bone replacement materials are generally categorized as osteoconductive, osteoinductive, and osteogenic. Osteoconductive materials are scaffolds allowing ingrowth of bone cells which eventually initiate new bone formation. Osteoinductive materials stimulate the transformation of bone cells into bone-building osteoblasts, for example by bone morphogenetic proteins. Osteogenetic materials moreover contain vital osteoblasts [61].

### *2.2.1 Natural bone replacement materials*

Natural bone replacement materials can be from autogenic, allogenic, or xenogenic sources [31, 62-64].

Autogenic material is bone transplanted in the same patient from one body part to another. As an osteogenic material containing living cells from the same body it is incorporated without difficulty and there is no risk of rejection. However, this procedure generates an additional wound which adds to the discomfort for the patient and eventually causes unaesthetic scars. Furthermore additional blood loss and prolonged anaesthetic time increases surgical risk. Donor sites are also limited as only few non-essential bones exist in the human body [63].

Allogeneic bone is of human source, but not taken from the same patient but from other individuals. It can be taken from dead and living donors. Living donors are for example patients receiving total hip replacement as the surgeon has to remove bone. The harvested bone is either employed unprocessed (frozen) or processed (freeze-dried). Unprocessed bone bears the risk of infection which can be foregone by the usage of processed bone which is free of bone marrow and protein. But processing leads to loss of osteoinductive properties. It is also less stable than unprocessed bone [31, 63].

Up to date in 90% of all bone replacement surgery world-wide either autogenic or allogenic bone is used [31].

Xenogenic material is bone from other species than human. It is freeze-dried or deproteinized before usage. Deproteinized bone from bovine source is the most common type. It is for example marketed as Bio-Oss® (Geistlich AG, Switzerland). Organic material is removed from the bovine *Spongiosa* by heating and chemical treatment with sodium hydroxide. Bio-Oss® is marketed as granules and block material (Figure 2-3). Due to its low mechanical stability it is applied as bone filler in cases requiring only few supporting function. Other bone replacement materials of bovine origin are Osteograf® (Dentsply, Germany) and Cerabone® (botiss biomaterials GmbH, Germany). Processed bone of equine or porcine origin is also marketed (for example Osteobiol®, Tecnoss, Italy) [31].

Bone from allogeneic and xenogeneic sources can also be demineralized by acid extraction. Though this process leads to loss of mechanical stability, the material retains osteoconductive and osteoinductive properties. It is inserted in cases requiring fast revascularization and without the need of any mechanical support [31].

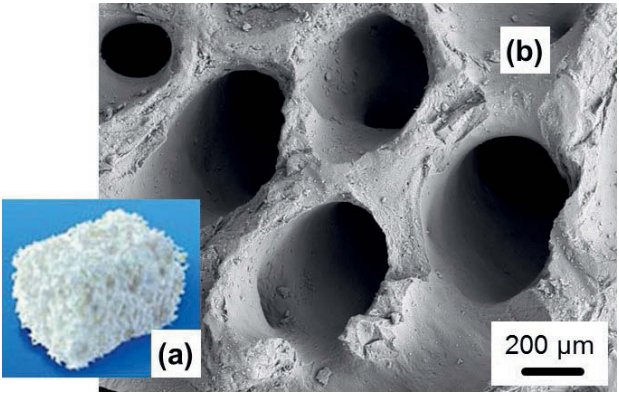


**Figure 2-3. Bio-Oss® by Geistlich AG: (a) block material as photographed, (b) microstructure as visualized by scanning electron microscopy**

### *2.2.2 Synthetic bone replacement materials*

Due to limited availability, risk of rejection and disease transmission, short shelf life, and low mechanical stability of natural bone replacement materials current research focuses on the development of synthetic bone replacement materials.

Suitable synthetic raw materials can be metallic, ceramic, or polymeric [31]. The most prevalent metal for bone replacement surgery is titanium. It is low-corrosive and

biocompatible as it is non-toxic and not rejected by the human body. It is commonly used as alloy including aluminium and vanadium (90Ti-6Al-4V) in which form it is considerably more mechanically stable than pure titanium oxide. Titanium alloys are preferably used for hip and knee replacements as well as dental implants where high mechanical stability is required. Titanium bone replacement materials are not osteoconductive but are often described as osteointegrative due to the good attachment of bone cells on the titanium surface. As remodelling in the human body is impossible the material is weakened over-time and implants must be substituted after periods of 20 to 30 years [65].

Some non-toxic polymers are also suitable bone replacement materials. The polymeric structure is similar to the structure of natural collagen and the properties of polymers are therefore to some extend similar to collagen for example regarding elasticity. A few polymers are even degradable in the human body as for example polylactide and polyglycolide. However degradation rates of 1 to maximal 6 month are much faster than of natural bone. This behaviour can be useful for drug release applications but may provide difficulty for bone remodelling as the material degrades faster than new bone can be formed [66]. Furthermore inflammatory response of bone tissue by degradation products is not uncommon and effects up to 5% of patients supplied with degradable polymeric implants [5].

Ceramics, glasses, and glass ceramics suitable as bone replacement materials are notably zirconium oxide (zirconia), aluminium oxide (alumina), calcium phosphates, and calcium-containing glasses and glass ceramics [58, 64].

Zirconia and alumina are the only metal-free materials that have sufficient strength to be applied for hip prostheses or dental implants [67]. In particular yttrium-stabilized zirconia (Y-TZP) unites high flexural strength with high fracture toughness. This is explained by the transformation toughening mechanism of Y-TZP. The low-temperature modification of zirconia is monoclinic. Above 1170°C it modifies to tetragonal zirconia. But the inclusion of yttrium ions into the structure effectuates the transformation to metastable tetragonal zirconia at low temperature. However when exposed to stress the tetragonal zirconia transforms locally to the stable monoclinic zirconia. This is accompanied by volume expansion, as the packing efficiency of the monoclinic phase is not as high as of the tetragonal phase. Thereby cracks induced by stress are stopped. Both alumina and zirconia are biocompatible but biologically inactive (bioinert) as there is no bonding to osseous tissue [67, 68].

Some glasses and glass ceramics of the $SiO_2$-$Na_2O$-CaO-$P_2O_5$-system are known to be bioactive, the most well-known type being the so-called Bioglass® [58]. When inserted an apatite-layer forms on the bioactive glass surface which enables bonding to osseous tissue. But a draw-back is the low bending strength of around 50 MPa. Apatite-Wollastonite glass ceramics which are as well bioactive have higher bending strength of around 200 MPa [69].

Calcium phosphates possess the closest resemblance to the chemical composition of bone mineral. Therefore numerous calcium phosphate bone replacement materials can be found on the market today. Most are granule or block variants of hydroxyapatite (HAp) or tricalcium phosphate (TCP) or a combination of both resulting in biphasic calcium phosphate (BCP). They are not only bioactive but resorbable. As HAp has a lower resorption rate than TCP the resorption rate can be influenced by the HAP:TCP ratio of BCP. However a problem is that the strength of calcium phosphate bone replacement materials is still considerably lower than of *Compacta* so that it can only be applied for substitution of *Spongiosa* [5].

## *2.3 Biofunctionalisation of bone replacements*

To actively promote bone healing, and not simply provide stabilisation, bone replacement materials can be functionalized with therapeutically active agents, most importantly agents stimulating bone growth and agents preventing infection [60].

Agents stimulating bone growth are called bone morphogenetic proteins (BMPs). They are able to induce osteoblastic differentiation by expression of the osteoblastic markers alkaline phosphatase and osteocalcin [70].

Agents preventing infection and supressing inflammatory reactions are above all antibiotics. But also some proteins are antibacterial active, for example antimicrobial peptides [71] or lysozyme [47].

Methods for administering drugs can be divided into two categories: systemic and local. Systematic drug delivery describes the conventional methods for drug delivery: oral administration and injection. Oral administration is generally seen as the most convenient method for the patient. However, it is not effective for all kind of drugs but limited to small molecules (for example antibiotica and steroid hormones). To administer macromolecular drugs such as proteins, protein hormones, and enzymes

systematically they must be injected which in most cases cannot be done by the patient himself [10-12].

The drawback of systematic administration is that it cannot ensure a sufficient concentration and efficacy at the defect site. Moreover, there can be toxic side effects on healthy body parts and the risk of overdose as the drugs are distributed throughout the body via the blood circulatory system [13, 14].

These disadvantages can be prevented by local drug delivery where medication can reach the targeted site more effectively. It moreover permits controlled delivery at a specific rate and for a specific period of time at the desired location.

The scaffold into which the drug is loaded as well as the applied loading method both determine the rate and manner in which a particular drug is released. The most common approaches for drug immobilisation in synthetic scaffolds are adsorption, chemisorption, and covalent attachment. By the adsorption mechanism molecules are attached on inorganic surfaces by electrostatic attraction and Van-der-Waals forces. When the adsorption is followed by the reaction of the molecule with the surface, forming a chemical bond, one speaks of chemisorption. Covalent attachment means attachment of drugs on inorganic surfaces by linker molecules. The amount of immobilised drugs that can be deposited on the surface is limited by the pore size and surface area of the scaffold [48, 49].

## *2.4 Calcium phosphates*

As described previously in chapter 2.1, bone consists of a unique calcium phosphate variant found nowhere else in nature: a calcium-deficient carbonated hydroxyapatite. For mimicking bone, various naturally occurring or synthetically fabricated calcium phosphates are applied, hydroxyapatite and tricalcium phosphate variants being the most prevalent.

### *2.4.1 Hydroxyapatite ($Ca_5(PO_4)_3OH$)*

Hydroxyapatite can be found in natural mineral deposits but is mainly occurring naturally in vertebrates as mineral in bone, dentin and enamel [59, 72].

Hydroxyapatite can be synthetically fabricated by wet chemical precipitation, for example of solutions of calcium nitrate ($Ca(NO_3)_2$) and diammonium phosphate ($(NH_4)_2HPO_4$) or alternatively calcium hydroxide ($Ca(OH)_2$ and phosphoric acid

($H_3PO_4$). It can also be prepared via sol-gel-process using for example calcium diethoxide and triethyl phosphate [73].

Hydroxyapatite typically forms on some materials, including silica, titania, and some calcium containing glasses, when immersed in simulated body fluid (SBF) which is an inorganic salt solution with ion concentrations equal to human blood plasma. These materials are referred to as bioactive [74].

Figure 2-4 shows the hexagonal crystal structure of hydroxyapatite.

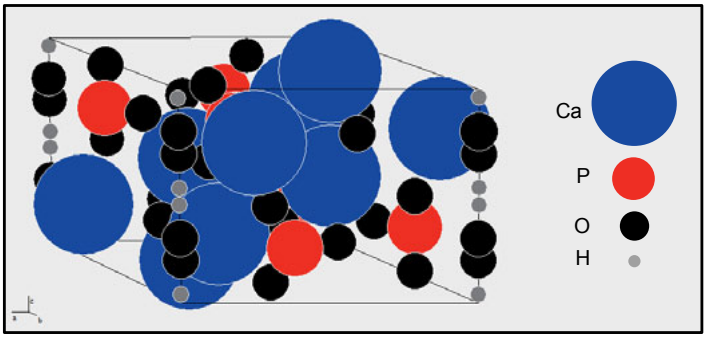


**Figure 2-4. Crystal structure of hydroxyapatite (constructed by PowderCell 2.3 [75] using data from reference [76])**

### *2.4.2 β-Tricalcium phosphate ($\beta$-$Ca_3(PO_4)_2$)*

β-Tricalcium phosphate can be rarely found naturally in rocks. It does not occur in living organisms. Its mineralogical name is Whitlockite.

β-tricalcium phosphate can be prepared by wet precipitation of a Calcium-deficient apatite and subsequent calcination at temperatures over 750°C [59, 77].

Figure 2-5 shows the trigonal crystal structure of β-tricalcium phosphate. There is a high temperature phase, monoclinic α-tricalcium phosphate, formatting from β-tricalcium phosphate at temperatures above 1125°C [72].

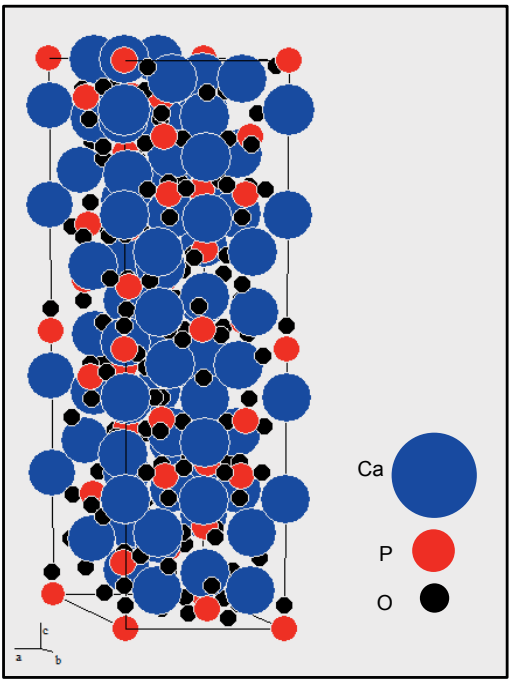


**Figure 2-5. Crystal structure of β-tricalcium phosphate (constructed by PowderCell 2.3 [75] using data from reference [78])**

## *2.5 Proteins*

Proteins are macromolecules consisting of amino acids which perform manifold functions in organisms. As the structure of proteins is complex it is broken down to primary, secondary, tertiary, and quaternary structure. The primary structure is the sequence of the 20 different amino acids. As secondary structure the arrangement of the amino acid chains is described which form sub-structures by hydrogen-bonding, as so-called α-helices and β-sheets. The tertiary structure is the three-dimensional shape of a polypeptide chain generated by the interaction of polar, apolar, acidic, and basic amino acids. A protein can consist of only one polypeptide. But commonly there are two or more polypeptide chains which is described by the quaternary structure.

Depending on the number of polypeptides proteins consisting of more than one polypeptide are referred to as dimers, trimers, tetramers, or oligomers [79].

According to their structure proteins are classified into four main types: globular, fibrous, membrane and disordered proteins.

Globular proteins are folded in spherical shape. They are in some degree water-soluble as the hydrophobic amino acids are mainly located inside the globular structure whereas the hydrophilic amino acids are mainly located outside. They are performing among others catalytic, transporting, and message transmitting functions.

Fibrous proteins have a wire-like shape and form so-called filaments. They built up tissues and have supporting function in the organism. They are water-insoluble and much more stable than globular proteins.

Membrane proteins are forming cell membranes. Disordered proteins have in contrast to the other protein types no ordered three-dimensional structure [20].

Relevant bone proteins besides collagen type 1 are the proteins that are involved in bone remodelling. Collagenase is an enzyme that breaks the peptide bonds of collagen. Bone morphogenetic proteins (BMPs) are directly inducing bone formation or regulating processes important for bone formation [80]. Other proteins involved in bone formation are osteonectin, thrombospondin, fibronectin, and osteocalcin [60].

However, for this work, proteins well investigated, easily available in considerable amounts, and with simple structure were needed. Therefore two at neutral pH oppositely charged model proteins, bovine serum albumin (BSA) and lysozyme (LSZ), were chosen to be useful for a variety of applications.

### *2.5.1 Bovine serum albumin (BSA)*

Serum albumin is a blood plasma protein serving transport functions. It has a globular structure and consists of several α-helices. It typically forms dimers. Its structure enables serum albumin to bind a variety of ligands at the same time. It has several binding sites for hydrophobic compounds, fatty acids and metal ions. Serum albumin has good water solubility. In human blood the solubility is 35 – 50 g/L. Common types for lab testing are human serum albumin (HSA) and bovine serum albumin (BSA) which was chosen in this work for its availability and low cost. The molecular weight of BSA is 68 kDa and its size 5x5x9 nm. The IEP of BSA is 4.7 to 5.3 which means that it is negatively charged at neutral pH [81]. Figure 2-6 illustrates the structure as well as the surface charge of BSA.

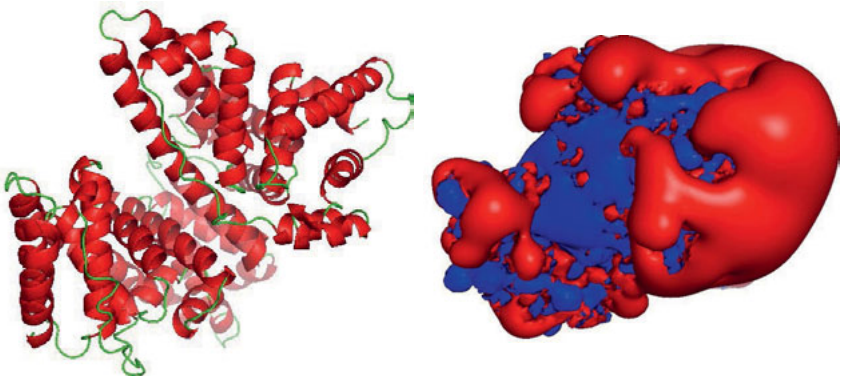

**Figure 2-6: Serum albumin: Images show the protein structure (left) and the distribution of positive (blue colored) and negative (red colored) surface charges (right) [82, 83]**

### *2.5.2 Lysozyme (LSZ)*

LSZ is an enzyme with antibacterial effect. For protecting the human body of infection it is present in secretions like saliva, blood, and tear fluid. It can destroy bacteria by damaging their cell walls but is only effective against gram-positive bacteria. Its antibacterial activity can be easily verified in microbiological lab tests [47].

LSZ has a globular structure and is very small. It consists of only 129 amino acids, has a molecular weight 14.3 kDa and its size is 3x3x4.5 nm. The IEP of LSZ is 10.7-11.3 which means that it is positively charged at neutral pH. It is water soluble but to less extend than serum albumin [84]. Figure 2-7 illustrates the structure as well as the surface charge of BSA.

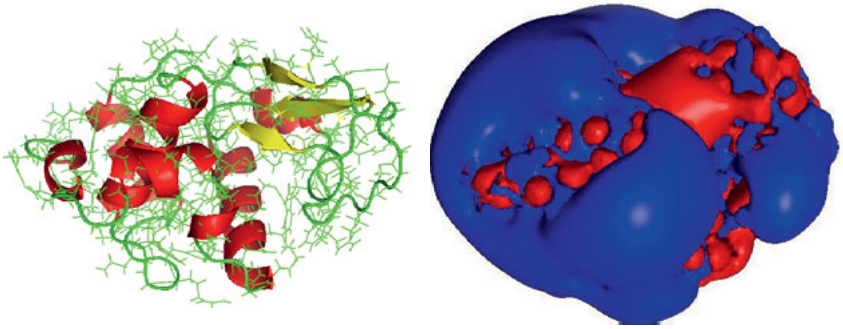

**Figure 2-7: Lysozyme: Images show the protein structure (left) and the distribution of positive (blue colored) and negative (red colored) surface charges (right) [82, 83]**

# 3 Methods

## 3.1 Powder characterisation

The following section gives an overview on methods for the characterisation of the raw powder materials used in this work.

### 3.1.1 Zeta potential

The stability of suspensions (solid/liquid-dispersions) can be estimated using zeta potential measurements. A stable suspension with low particle agglomeration and sedimentation tendency is crucial for wet-route scaffold fabrication processes.

When particles are submerged in liquid, positively and negatively charged ions in the liquid are attracted depending on the particle's surface charge. They form the so-called Stern layer directly on the particle surface, a monolayer of ions oppositely charged to the particle surface. Further ions are assembled in vicinity of the Stern layer forming the diffuse double layer of mainly oppositely-charged but also a few like-charged ions. The surface potential $\psi_0$ cannot be measured directly. However the zeta potential $\psi_\zeta$ on the shear plane between stern layer and diffuse double layer can be measured to quantify the particle charge (Figure 3-1) [85].

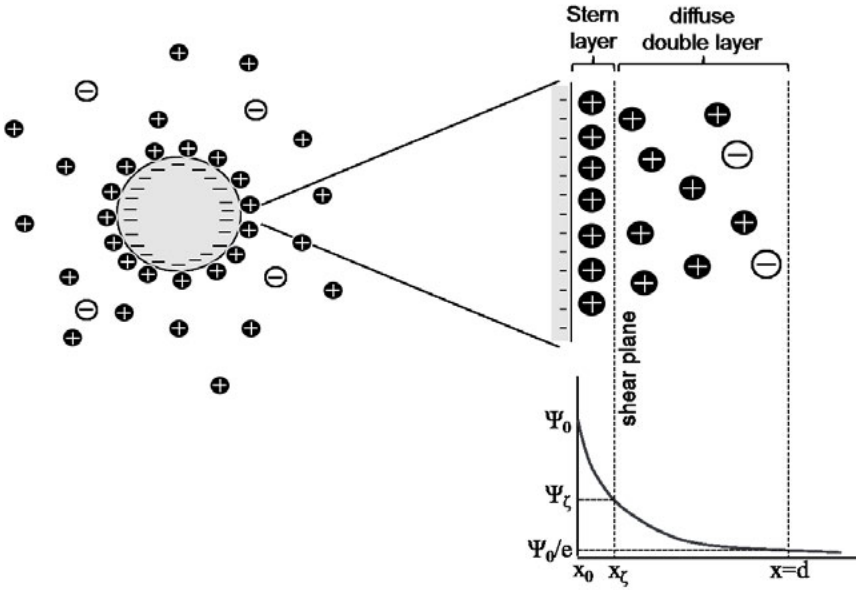


**Figure 3-1. Schematic of the diffuse double layer around a particle. The zeta potential is located on the shear plane. Illustration based on Salmang & Scholze, Keramik, p. 572 [85]**

The zeta potential of a particle suspension is influenced by pH and ionic strength. When the medium pH changes the particle surface will get predominantly protonated, neutral, or deprotonated. The medium pH at which the particle surface charge is neutral is called the isoelectric point (IEP). At the IEP the surface potential is zero. Thus the suspension is not stable as particles are not repelled from each other.

The suspension is also unstable at high ionic strength. As the zeta potential is the potential difference of particle surface charge and medium the zeta potential decreases with increasing ionic strength. Only at low ionic strength the surface potential and zeta potential can be considered as almost equal [86].

There are two techniques for the measurement of the zeta potential in suspensions with high particle volume fraction: colloidal vibration potential (CVP) [87] and electrokinetic sonic amplitude (ESA) [88].

When using colloidal vibration current technique the particles and ions in suspension are initiated to move by ultra sound. The current (CVP) generated thereby

is than measured between two electrodes [87]. CVP is linked to the dynamic electrophoretic mobility over the following equation:

$$CVP = C' \cdot \varphi \cdot \mu_e \cdot \frac{\rho_p - \rho_m}{\kappa^* \cdot \rho_m} \cdot \frac{Z_g' \cdot Z_s'}{Z_g' + Z_s'}$$

| | | |
|---|---|---|
| *with* | $C'$, | *calibration constant* |
| | $\varphi$ | *volume fraction* |
| | $\mu_e$ | *dynamic electrophoretic mobility* |
| | $\rho_p$ | *density (particle)* |
| | $\rho_m$ | *density (medium)* |
| | $\kappa^*$ | *complex conductivity of dispersed system* |
| | $Z_g$, $Z_s$ | *acoustic impedances of the sound transducer and the dispersed system* |

For the electric sonic amplitude (ESA) an oscillating electric field is applied by two electrodes [88]. By this electric field the particles are moved which generates ultrasound. ESA is also linked to the dynamic electrophoretic mobility:

$$ESA = C \cdot \varphi \cdot \mu_e \cdot \frac{\rho_p - \rho_m}{\rho_m} \cdot \frac{Z_g \cdot Z_s}{Z_g + Z_s}$$

Knowing the dynamic electrophoretic mobility the zeta potential can be calculated by Henry's equation [85].

$$\mu_e = \frac{2}{3} \cdot \frac{\varepsilon \cdot \varepsilon_0 \cdot \zeta}{\eta} \cdot f(\kappa a)$$

| | | |
|---|---|---|
| *with* | $\eta$ | *viscosity of the medium* |
| | $\varepsilon$ | *relative dielectric permittivity of the medium* |
| | $\varepsilon_0$ | *permittivity of vacuum* |
| | $\kappa$ | *Debye-Hückel parameter* |
| | $\alpha$ | *particle radius* |
| | $\zeta$ | *zetapotential* |
| | $f(\kappa\alpha)$ | *Henry's constant* |

However Henry's equation assumes spherical particles. It must be considered that most powders do not consist of perfectly spherical particles.

### *3.1.2 Particle size measurement*

The simplest method for estimating the particle size of powders is sieving. However sieving only allows separation in particle size fractions depending on the number of differently mesh-sized sieves applied.

Methods yielding more exact particle size distributions are electroresistance counting, laser diffraction and acoustic spectroscopy. An example for electroresistance counting is the Coulter counter where particles are separately pulled through an orifice under electric current. Thereby the particle size can be evaluated as the change in impedance is proportional to the particle volume [85].

Laser beams as well as ultrasound waves are absorbed and scattered by particles in suspensions. This principle is employed by laser diffraction and acoustic spectroscopy. By laser diffraction methods the particle size distribution is assessed by the angular variation of the intensity of light [89] whereas by acoustic spectroscopy the frequency spectrum generated by the attenuation of ultrasound is analysed [87].

### *3.1.3 Density*

The density of powders can be determined by liquid or gas pycnometry. If a known amount of powder is dispersed in a known volume of water the particle density can be calculated. The exact density of water at the temperature of suspension can be taken from literature [90].

Gas pycnometry is working according to the same principle. However, a gas-tight apparatus is required. Usually gas pycnometry is conducted with helium as the gas molecules are extremely small, filling even the smallest particle surface cavities. Moreover, helium is an inert gas [91] that does not chemically react with the samples.

## *3.2 Scaffold fabrication*

This chapter describes methods for the fabrication of open-porous scaffolds.

### *3.2.1 State of the art*

Methods to produce open-porous scaffolds are replica techniques, direct foaming, and freeze casting [15-17].

Replica techniques use synthetic or natural foams as templates which are immersed in suspensions or precursor solutions. Subsequently the foam is burned and only the ceramic scaffold remains as a negative replica of the foam. Suitable foams are polymer sponges, carbon foams, corals, and wood. The method was established in the 1960s by Schwartzwalder *et. al*. employing polyurethane sponges [92]. Open pore sizes achieved by replica technique are usually above 200 µm. However, as the struts are hollow and often partly damaged by pyrolysis it is difficult to fabricate strong scaffolds by replica techniques [17].

Direct foaming denotes that air bubbles are incorporated in a suspension and stabilized by surfactants. By subsequent drying a ceramic foam can be obtained [17, 93]. It is also possible to incorporate volatile oils instead of air, as for example short-chain alkenes which can be equally stabilized by surfactants [94]. With direct foaming it is possible to fabricate highly porous scaffolds with up to 90% porosity [94].

By freeze casting a water-ceramic-suspension is cast into a mould and frozen. Thereby, ice crystals grow and generate open-porous scaffolds. As ice has a higher volume than water the ceramic part is densified in addition [15, 95]. However, subsequent freeze drying and sintering is required to obtain a stable scaffold. Therefore a modified process variant, the freeze gelation process, is considered more feasible [28, 96].

### *3.2.2 Freeze gelation process*

The freeze gelation process is based on the freeze casting process following the same procedure as described above. However, a freeze-sensitive silica sol is added in addition to the ceramic suspension. A silica sol is a nanoparticle silica suspension. When frozen it is irreversibly transformed to a gel, solidifying the ceramic body which retains its shape and stability after melting of the ice [96]. Consequently a freeze drying

step can be foregone. As the dried green bodies have already a considerable strength it is moreover possible to skip sintering processes.

This allows the direct incorporation of heat-sensitive biomolecules and enables the one-step fabrication of open-porous ceramic/protein-scaffolds. As there are no harmful substances necessary for the freeze gelation process the fabrication of synthetic scaffolds likewise osteoconductive and osteoinductive is possible. The process is moreover near-net shape as casting of a suspension allows the fabrication of scaffolds in complex geometries.

As shown by Soltmann *et al.* it is moreover possible to directly incorporate living organisms as bacteria, spores, or yeast which in a large part survive the processing [96]. Therefore, this processing route eventually has the potential for the fabrication of synthetic osteogenic scaffolds containing vital osteoblasts.

## *3.3 Scaffold characterisation*

This chapter describes methods for the characterisation of scaffolds both regarding their material properties and biocompatibility.

### *3.3.1 Scaffold material properties*

#### *3.3.1.1 Porosity*

The total porosity of a specimen with defined geometry can be determined by measuring the sample weight and dimensions to calculate the volume. Knowing the raw material's density the total porosity can be assessed by the following equation:

$$\Phi_{Total} = 100 - \left( \frac{m_{sample} \cdot 100}{V_{sample} \cdot \rho_{material}} \right)$$

However by this simple method a distinction between open and closed porosity is not possible. Total open porosity, pore size distribution, and specific surface area can be assessed by using mercury intrusion porosimetry. Depending on the instrument pore sizes from 3.5 nm to 500 µm can be determined. Mercury is non-wetting to most solids. Therefore it can only be intruded into scaffolds by external pressure. By measuring the pressure which is needed to intrude and the intruded volume of mercury the pore size distribution of a scaffold can be determined [91].

The pore size and pore size distribution can also be assessed by microscopic methods (optical and scanning electron microscopy). Image processing software allows the measurement of pore sizes. However for quantification the evaluation of numerous images is necessary.

#### *3.3.1.2 Mechanical stability*

The mechanical stability is evaluated by determining the scaffold's resistance against tension and compression. There are several test arrangements considering compression (compressive strength), tension (tensile strength), or both (flexural strength).

Test set-ups to measure compressive strength are the simplest. However the material is deformed with increasing load and there is no clear fracture. Generally the load F at a specific deformation is measured to determine the stress σ knowing the cross-section area A of the specimen.

Tensile strength is measured by pulling a specimen apart. But to get exact results specimens must be ideally orientated in direction of the tension applied. Only minimal deviations in sample orientation can lead to high discrepancy in results.

As it unites accuracy with a relatively easy test set-up the most prevalent test method for brittle materials is flexural strength. For this test flat specimens are bended by applying punctual load on the top side. Thereby, the specimen gets under compression at the top side and under tension at the bottom side. As most materials can withstand higher compressive strength than tensile strength the fracture typically starts from the bottom side of the specimen.

Prevalent test set-ups for measuring the flexural strength are 3-point bending, 4-point bending, and biaxial flexure strength. The uniaxial 3- and 4-point bending tests are conducted with beam geometries. Both set-ups use two support rollers at the bottom. But whereas for 3-point bending load is applied by one roller in the middle for the 4-point set-up load is applied by two loading points on the topside (Figure 3-2) [85, 89].

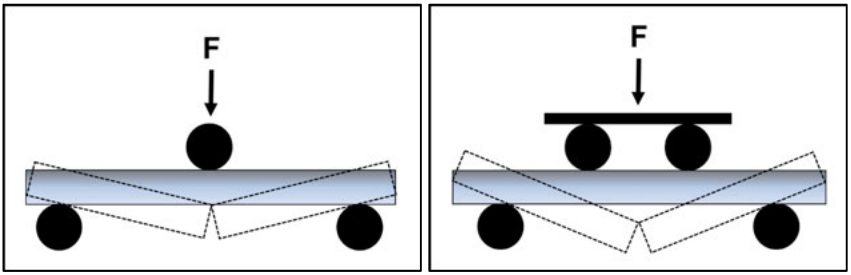


**Figure 3-2. Schematic of three and four point bending test set-up.**

Biaxial test set-ups are more sensitive to material defects than uniaxial test set-ups and tolerate inaccuracies in sample geometry to a much higher extend [97]. Biaxial testing requires disc shaped specimens. There are test set-ups with ring support or support with (usually three) balls [89]. For this work the ball-on-three-balls test was applied where the sample disc is supported by three metal balls arranged in a circle and punched by one ball from above situated in the middle of the disc (Figure 3-3). The biaxial flexure strength can be calculated according to the following equation as reported by Shetty *et al*. [98].

$$\sigma_{\max} = \frac{3 \cdot F \cdot (1+\nu)}{4 \cdot \pi \cdot t^2} \times \left[ 1 + 2 \cdot \ln\left(\frac{r_a}{b}\right) + \frac{(1-\nu)}{(1+\nu)} \cdot \left(1 - \frac{b^2}{2 \cdot r_a^2}\right) \cdot \frac{r_a^2}{r^2} \right]$$

*with* $F$, *applied load*

$\nu$, *Poisson's ratio of the disc material*

$t$, *sample thickness at centre*

$b$, *contact ratio of the loading ball assumed to equal t/3* [98]

$r$, *radius of the disc*

$r_a$, *support radius of the 3 supporting balls*

The material-specific Poisson's ratio can be taken from reference. The Poisson's ratio for porous HAp ceramics is 0.25 [99].

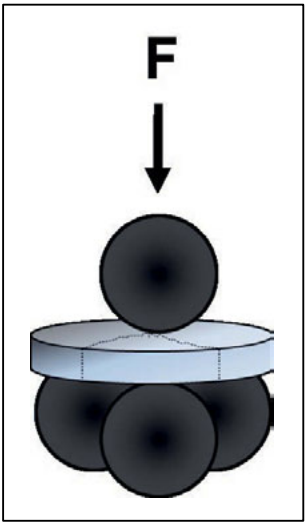


**Figure 3-3. Schematic of the ball-on-three-balls test**

### *3.3.2 Scaffolds' biocompatibility*

#### *3.3.2.1 Ultraviolet-visible spectroscopy (UV/VIS)*

Ultraviolet-visible spectroscopy is an adsorption spectroscopy method for the quantification of solved or dispersed inorganic or organic compounds. In general the measurement is conducted at a specific wavelength which is significant for the adsorption of the substance of interest. For measurement liquids are put into so-called cuvettes which are transparent in the required spectral region. For VIS spectroscopy plastic cuvettes of poly(methyl methacrylate) are sufficient. For UV spectroscopy silica glass cuvettes are required. It is possible to measure the transmittance or absorbance (optical density). The adsorption of most inorganic and organic compounds is not high enough, especially at low concentrations, to produce a measurable signal. Therefore, in most cases, dyes procuring a colour change dependent on concentration are added. For quantification it is necessary to firstly generate standard curves of known compound amounts [100].

The most common method to assess protein concentrations in solution by UV/VIS is the Bradford assay. The chemicals involved in the Bradford assay procure a colour change dependent on amino acid composition of the protein. The dye used is

Coomassie Brilliant Blue G-250. Under acidic condition the brownish dye is converted to blue when binding to protein. The adsorption spectrum maximum of the reacted blue dye is at wavelength 595 nm where transmittance is measured. Bradford reagent can be obtained as ready-to-use product that can be mixed directly with the sample. It is possible to measure protein concentrations as low as 1 µg/ml. The accuracy of the Bradford assay is not interfered by most buffers, solvents, salts, preservatives, or metal chelating agents. As a drawback the Bradford assay is only linear over a short concentration range. Therefore oftentimes dilutions of the sample are necessary to fit the standard curve [101].

Calcium content in solution can be assessed by using an o-cresolphthalein complexone assay. When $Ca^{2+}$ ions react with o-cresolphthalein complexone in an alkaline solution an intense violet coloured complex is formed. The adsorption spectrum maximum is at wavelength 577 nm where transmittance is measured. O-cresolphthalein complexone assay can also be obtained ready-to-use. The measurement limit is 0.05 mmol/l [102].

UV/VIS can be applied for the determination of the bacteria number in liquid. To assess bacteria number standard solutions called McFarland turbidity standards, referring to the inventor, are applied. The common McFarland standards 0.5, 1, 2, 3, and 4 correspond to bacteria cell densities of 1.5, 3.0, 6.0, 9.0 and 12.0 x 10^8 CFU/ml (colony forming units per ml). McFarland standards were originally prepared by barium chloride and sulfuric acid which form a barium sulfate causing turbidity in solution [103]. Today more advanced and durable McFarland turbidity standards are prepared by particle suspensions [104]. McFarland turbidity standards can be purchased ready-to-use.

#### *3.3.2.2 In vivo experiments*

Biocompatibility and resorption behaviour can be partly assessed by *in vitro* experiments. However, to draw definite conclusions *in vivo* experiments are required. The animal model used in this work is the forehead region of pigs. It shows similar bone regeneration rates (1.2-1.5 µm/day) as compared to humans and therefore provides ideal conditions for studying bone regeneration and implant osseointegration [105, 106].

As appropriate scaffold geometry cylindrical shapes with dimensions of 14 mm in length and 10 mm in diameter and rounded off on one end were used. This scaffold shape is on one hand founded on the fit to the defect site of 10 mm in diameter and 10 mm in depth created by a trephine burr [105, 106]. On the other hand its oversize and rounding off is required to elevate the local periosteum and aims to generate additional bone above the samples [107] (Figure 3-4).

**Figure 3-4. Scaffolds fabricated for *in vivo* experiments**

After sacrificing the animals scaffold resorption and new bone formation can be visualised by microradiographic and light microscopic evaluation. Obtained microradiographic images can be analysed by software [108] to quantify material persistence and new bone formation.

#### *3.3.2.3 Antibacterial properties*

Typical methods to assess the antibacterial properties of scaffolds are optical density measurements, total viability counts, and zone of inhibition tests (Kirby-Bauer tests).

Antibacterial tests always start with the cultivation of bacteria. Normally bacteria are first cultivated on agar plates. Agar plates are petri dishes layered with agar enriched with nutrient. Afterwards the cultivated bacteria can be suspended in nutrient broth for proliferation. The bacteria cell density after proliferation can be determined by

optical density measurements using McFarland turbidity standards (see chapter 3.3.2.1).

Obtained bacteria solutions of known cell density can be applied for experiments to determine the antibacterial properties of scaffolds. For example scaffolds can be submerged in bacteria suspension. The bacteria activity after contact with antibacterial materials can be quantified by optical density measurements or total viability counts.

For total viability counts bacteria solution is spread on agar plates with a Drigalski spatula, an instrument applied to spread bacteria uniformly on the agar plate. After a suitable cultivation time the number of colony forming units (CFU) on the agar plate can be counted. On the one hand there must be enough CFUs to make the test statistically relevant. On the other hand, if there are too many CFUs the method will be less exact as single CFUs cannot be discerned anymore. Therefore generally several dilutions must be performed to get a usable result [109].

The Kirby-Bauer test, also not directly yielding the number of dead or living cells, is a very reliable test to determine the ability of probed samples to inhibit microbial growth. For this test an antimicrobial sample will be placed in the middle of an agar plate on which bacteria are dispersed for cultivation. If the bacteria strain is susceptible to the antimicrobial sample a clear zone, the zone of inhibition, will appear on the agar plate around the sample. The extension of the zone of inhibition which can be measured is dependent on the amount and antimicrobial efficacy of the agent [110].

# 4 Experimental

Parts of this chapter have been published in Advanced Engineering Materials, 2010 (Vol. 12, I. 1-2, p. B53-61) and in Materials Science and Engineering: C, 2014 (Vol. 42, p. 137-145).

## 4.1 Characterisation of calcium phosphate powders

Calcium phosphate powders were obtained commercially, HAp powder from Riedel-de Haën (04238, lot no. 70080) and the β-TCP powder from Fluka (21218, lot no. 1305078). The crystal structure of the calcium phosphate powders was confirmed by X-ray powder diffraction (Debey Isoflex 2002, GE Inspection Technologies). The density of the powders was measured by helium pycnometry (AccuPyc 1330, Micromeritics). The calcium phosphate particle size distribution was measured by ultrasonic spectroscopy [87] (DT 1200, Dispersion Technology) and the specific surface area was quantified by BET (Gemini, Micromeritics). The particle shape was defined by SEM images (Cambridge Scan, Cambridge Instrument Company) and in the case of the HAp powder also TEM images (CM 20 UT, Phillips). (SEM/TEM images: see appendix A).

The $Ca^{2+}$-solubility against pH was measured using a $Ca^{2+}$-ion-selective microelectrode (MI 600) combined with a reference electrode (MI 409) and a pH microelectrode (MI 410) purchased from Microelectrodes Inc. Suspensions of the calcium phosphate powders with a total sample volume of 5 to 10 mL were prepared using double deionised water. The powder concentration of the samples was 6 vol%. The pH was adjusted using 1 M HCl and 1 M KOH. The addition of acid and base changed the initial powder concentration down to 5 vol% and at low pHs < 4 even down to 3 vol%. After 72 hrs of mixing, the samples were centrifuged and the $Ca^{2+}$-concentration and pH of the supernatants measured simultaneously. Each solution was measured 5 times and hereafter the concentrations corrected taking into account the added acid and base volumes.

## *4.2 Combined zeta potential / VIS spectroscopy measurements*

### *4.2.1 Material*

The HAp powder was purchased from Riedel-de Haën (04238, lot no. 70080) and the β-TCP powder from Fluka (21218, lot no. 1305078). The powders were sterilised thermally at 200°C for 2 hrs.

The proteins, albumin from bovine serum (A7906, lot no. 036K0722) and lysozyme from chicken egg white (L6876, lot no. 027K1405), were purchased as dry powder from Sigma Aldrich. The characteristics of BSA and LSZ according to literature are summarized in Table 4-1.

For preparing the suspensions double deionised water with an electrical resistance of 18.2 MΩ cm was used, supplied from an ultra-pure water system (Synergy system, Millipore). The pH was varied by addition of 1 M KOH and 1 M HCl solution, respectively, both purchased from Fluka. A colorimetric assay based on the Bradford reaction was obtained from Bio-Rad (500-0006, lot no. 106276).

**Table 4-1. Protein Data (taken from indicated references)**

| | Mw [kDa] | Size [nm] | | Isoelectric point at pH |
|---|---|---|---|---|
| | | Side-on area | End-on area | |
| BSA | 68.0 [84] | 5x9 [36] | 5x5 [36] | 4.7-5.3 [33, 84] |
| LSZ | 14.3 [84] | 3x4.5 [36] | 3x3 [36] | 10.7-11.3 [84, 111, 112] |

### *4.2.2 Methods*

The protein concentration in the powder suspensions was normalized to the powder surface area to allow the comparison of the two calcium phosphate powders. 1 vol% powder suspensions with 0, 25, 50, 100, 200, 400, 800 and in some cases 600 ng/cm² protein content were prepared. However, due to the higher surface area of the HAp powder this proceeding leads to considerably higher protein concentrations in the HAp powder suspensions as compared to β-TCP powder suspensions.

First the powder was mixed with four fifth of the required water amount and deagglomerated for 8 min by using an ultrasonic horn (Sonifier 450, Branson). The fifth part of water was used to pre-dissolve the protein. After addition of the protein solution

the powder suspension was stirred for 16 hrs for equilibration. Each preparation volume of 100 mL was sufficient for two independent zeta potential and the VIS spectroscopy measurements.

The zeta potential was detected by colloidal vibration current technique [87] with a device (DT 1200, Dispersion Technology) that allows the concurrent measurement of zeta potential, conductivity (detection limit >0.0001 S/m ±1%) and automatic titration. For each preparation two measurements were conducted, one acidic and one alkaline titration. The powder suspensions were stirred strongly throughout the measurement in order to prevent sedimentation.

In order to prepare the samples for VIS spectroscopy the suspension was centrifuged two times for 10 min at 3800 g in a microcentrifuge (Fresco 21, Heraeus) at room temperature. VIS adsorption was subsequently measured with a photometer at a wavelength of 595 nm (Xion 500, Dr. Lange GmbH) by adding Bradford reagent to the supernatant of the suspension [101]. The protein concentrations of the supernatants were determined using a calibration curve of known protein concentrations. The supernatant protein concentration was used to calculate via mass-balance the amount of protein adsorbed on the powder surface.

## *4.3 Scaffold fabrication by Freeze Gelation (FG)*

### *4.3.1 Materials*

Hydroxyapatite (HAp) powder with a particle size of 0.1 µm and a specific surface area of 65 g/m² (Cat No 04238), calcium chloride hexahydrate (Cat No 21110, potassium sulfate (Cat No P0772), phosphate buffered saline (PBS, Cat No P4417), albumin from bovine serum (Cat No A7906, purity > 98 %), porcine serum albumin (Cat No A1830, purity > 98%), lysozyme from chicken egg white (Cat No L6876, purity > 90 %) were purchased from Sigma Aldrich, Germany.

Ammonia stabilised silica sol with a $SiO_2$ content of 30% (particle size of 5–8 nm, specific surface area of 230–360 m²/g, BINDZIL® 30 NH3/220, lot. 0590b) was obtained from EKA Chemicals (Germany). Anhydrous citric acid (Cat No 27488) was purchased from Fluka (Germany). All chemicals were utilised as received without further purification.

Double-deionised ($ddH_2O$) water with a conductivity of 0.05 µS/cm obtained from an ultra-pure water system (Synergy system, Millipore, Germany) was used for all studies.

### *4.3.2 Methods*

The one-pot-process for the composite fabrication is schematically given in Figure 4-1 and the different composite types including compositions summarised in Table 4-2.

**Table 4-2. Composition of the fabricated composite types**

| Composite type | Composition [wt.% (vol.%)] | | | | |
|---|---|---|---|---|---|
| | HAp | Silica | Citric acid | BSA | LSZ |
| protein-free | 96.0 | 0.960 | 3.04 | 0 | 0 |
| HAp/BSA-1 | 95.0 | 0.950 | 3.01 | 1.0 (2.3) | 0 |
| HAp/BSA-5 | 91.0 | 0.912 | 2.89 | 5.0 (11.0) | 0 |
| HAp/LSZ-0.5 | 95.5 | 0.955 | 3.02 | 0 | 0.5 (1.2) |
| HAp/LSZ-1 | 95.0 | 0.950 | 3.01 | 0 | 1.0 (2.3) |
| HAp/LSZ-1.5 | 98.5 | 0.946 | 2.99 | 0 | 1.5 (3.4) |
| HAp/LSZ-2.5 | 97.5 | 0.936 | 2.96 | 0 | 2.5 (5.7) |
| HAp/LSZ-5 | 91.0 | 0.912 | 2.89 | 0 | 5.0 (11.0) |

Suspensions were prepared by first mixing 1wt. % of $SiO_2$ sol (gelling agent) with citric acid. Citric acid was added as dispersant to improve suspension stability and castability. The optimal amount of citric acid was determined by zeta potential and conductivity measurements detected by colloidal vibration current technique [87] with a device (DT 1200, Dispersion Technology, USA) that allowed automatic titration and the concurrent measurement of zeta potential and conductivity (DT 1200, Dispersion Technology, USA). Zeta potential and conductivity measurements were carried out with 1 vol.% HAp suspensions and different amounts of citric acid ranging from 0.1 to 1.5 mg/m² (Appendix B). A final amount of 0.5 mg/m² (normalised on the HAp powder specific surface) enabled good castability for both HAp suspensions with and without

proteins. Therefore, for all subsequent investigations the citric acid content of 0.5 mg/m² was kept constant.

After adjusting the pH to 8 with a concentrated ammonia solution, HAp powder (33 vol%) was mixed into the solution using a stirring device (Dispermat LC-2, VMA-Getzmann, Germany) and a stirring velocity up to 2000 rpm. According to preliminary measurements, this stirring velocity was selected as facilitated slurry processing and castability.

For the fabrication of protein-free composites, the suspension was kept afterwards on a rolling machine (UR-400-FU-EH, Germatec, Germany) to avoid sedimentation and used within 24 h and without any further modification.

For the fabrication of HAp/protein composites a similar protocol was employed. Lyophilised proteins were directly added to the HAp suspension and stirred for 5 min at a constant stirring velocity of 2000 rpm and then kept on a rolling machine and used within 24 h.

Subsequently, the slurries without and with proteins were casted into a mould made of unplasticised polyvinyl chloride and subsequently placed in a freezer at -150°C for 30 minutes. After demoulding the samples were immediately put in tightly sealed desiccators and kept at constant relative humidity (r. h.) of 97 % and at room temperature (25°C) for 1 week to prevent crack formation. After 1 week storage at these conditions, part of the composites were maintained at these conditions, whereas some composites were stored at 30 % r. h for a maximal storing time of 12 weeks. The different r. h.s were obtained using concentrated salt solutions of calcium chloride hexahydrate (Cat No 21110, Sigma Aldrich, Germany) for 30 % r. h. and potassium sulfate (Cat No P0772, Sigma Aldrich, Germany) for 97 % r. h.

For the scaffolds fabricated for antibacterial tests (results see section 5.3) the drying conditions were not varied. All composites of this study (with 0.5, 1.0, 1.5, and 2.5 wt.% LSZ and scaffolds without LSZ used as reference) were dried for 1 week at 97 % r. h. and subsequently for 12 weeks at 30 % r. h.

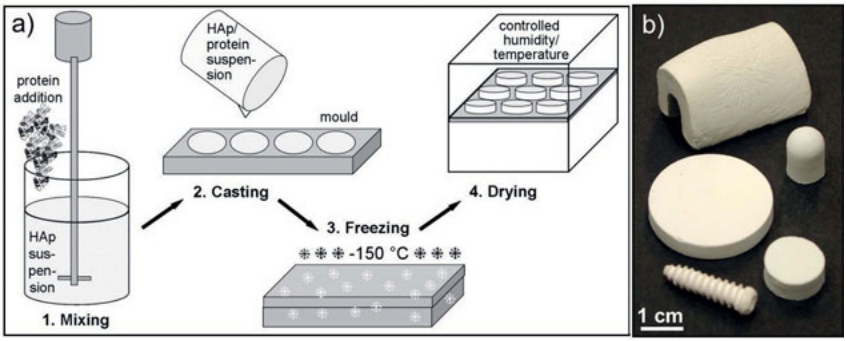


**Figure 4-1. (a) Schematic of the one-pot fabrication process for HAp/protein composites. First a HAp suspension is produced in which the protein is dispersed. Subsequently the HAp/protein suspension is cast into a mould and frozen at -150°C. Drying at controlled humidity and temperature conditions for 1 to 12 weeks completes the shaping process. (b) Selection of HAp/protein composite shapes that were obtained by the one-pot process. Sample shapes used for mechanical* and *in vivo*# testing are marked. Screw shaped samples see [30, 113]. This graphic was adapted from: Mueller, B.; Koch, D.; Lutz, R.; Schlegel, K. A.; Treccani, L.; Rezwan, K.; A novel one-pot process for near-net-shape fabrication of open-porous resorbable hydroxyapatite/protein composites and in vivo assessment. Materials Science and Engineering: C, 2014, Vol. 42, p. 137-145 (license number 4119440246729).**

## *4.4 Characterisation of HAp/protein composite structure*

The pore size distribution and the open porosity of the composites were measured by mercury intrusion porosimetry (Pascal 140/440, Porotec, Germany) to analysis pore ranging from 5 nm to 1 µm. Due to the limitation of this method, larger pores were therefore determined by analysing scanning electron microscopy images (Cambridge Scan, Cambridge Instrument Company, UK) with an image processing software (AxioVision Re. 4.8, AxioVision Microscope Imager, Zeiss, Germany). The total porosity ($\Phi_{total}$) of HAp/protein was calculated according to the following equation and using 50 specimens of each composite type.

$$\Phi_{Total} = 100 - \left( \frac{m_{sample} \cdot 100}{V_{sample} \cdot \rho_{material}} \right)$$

The volume ($V_{disc}$) and the weight ($m_{disc}$) of the cylindrical specimens were measured. Knowing the material density of the HAp powder [114] and the proteins [115], the material density $\rho_{material}$ for all composite types could be calculated dependant on their HAp/protein ratio.

## *4.5 Biaxial flexure strength testing*

For the ball-on-three-balls test disc-shaped samples shown in Figure 4-1b (* symbol) were supported by three metal balls arranged in a circle and punched by one ball from above situated in the middle of the disc (Figure 4-2). All balls were of equal size with a diameter of 17 mm. The experiments were conducted with a compression-tension testing machine (Zwick Z005, Zwick, Germany) and using specimens of 27.5 ± 1 mm in diameter and 4 ± 1 mm in thickness. The biaxial flexure strength was calculated according to the following equation as reported by Shetty *et al.* [98]. The Poisson`s ratio for porous HAp ceramics ($\nu$ = 0.25) was taken from Ren *et al.* [99].

$$\sigma_{\max} = \frac{3 \cdot F \cdot (1+\nu)}{4 \cdot \pi \cdot t^2} \times \left[ 1 + 2 \cdot \ln\left(\frac{r_a}{b}\right) + \frac{(1-\nu)}{(1+\nu)} \cdot \left(1 - \frac{b^2}{2 \cdot r_a^2}\right) \cdot \frac{r_a^2}{r^2} \right]$$

*with* $F$, *applied load*

$\nu$, *Poisson's ratio of the disc material*

$t$, *sample thickness at centre*

$b$, *contact ratio of the loading ball assumed to equal t/3* [98]

$r$, *radius of the disc*

$r_a$, *support radius of the 3 supporting balls*

The biaxial flexure strength was measured for specimens after 1, 3, 6, 9, and 12 weeks storage time and stored at 97 % and 30 % r. h, respectively. To exclude influences from the composites' water content, prior each measurement, samples were

stored at 37°C in a drying oven for 16 h. A drying temperature of 37°C was specifically chosen to prevent potential protein denaturation. Samples stored at 97 and 30 % r. h. had an equal sample weight after drying indicating equal residual water content in all cases and thus permitting comparable measurement conditions for all sample types. For all measurement points 5 samples were tested.

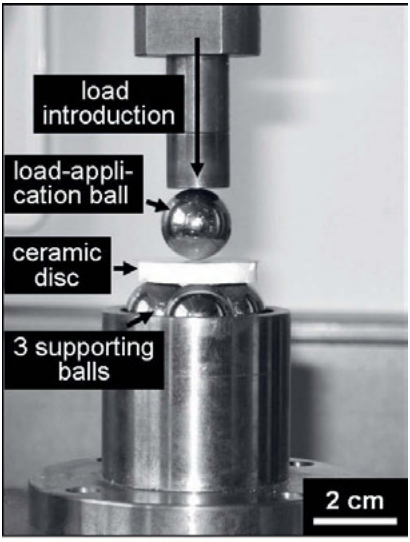


**Figure 4-2. Experimental set-up of the ball-on-three-balls mechanical test. For the biaxial flexure strength test according to Borger *et al.* [97] a ceramic disc is supported by three balls arranged in a circle and punched by one ball on top of the disc. The set-up allows a defined load introduction and minimises the influences of inaccuracies in sample geometry.**

## *4.6 Protein and $Ca^{2+}$ release measurements*

### *4.6.1 Quantification of release of HAp/protein scaffolds (for results see chapter 5.2)*

*In vitro* protein release was investigated by immersing samples with a weight of 1 ± 0.2 g in PBS buffer at 37°C and constantly shaken. For 0.1 g of sample 1 ml of PBS was added in order to keep the amount of liquid and the amount of protein in the sample at a constant ratio. After 168 hours (7 days) the protein concentration in the medium was measured using the Bradford protein assay (Cat No 500-0006, Bio-Rad, USA) according to supplier´s protocol [101]. Protein concentrations were measured with a VIS spectrometer (Xion 500, Dr. Lange, Germany) at a wavelength of 595 nm. The protein release of all protein-containing composites was measured for specimens after 1, 3, 6, 9, and 12 weeks storage time and stored at 97 % and 30 % r. h, respectively. The measurements were carried out in triplicate.

### *4.6.2 Release reference measurements under bacterial testing conditions (for results see chapter 5.3)*

The LSZ and $Ca^{2+}$ release was measured using cylindrical specimens of 14 mm in diameter and 5.5 mm in heights. The specimen were immersed in 8 ml PBS and 0.2 ml of supernatant was removed after 10 min, 30 min, 1 h, 2 h, 4 h, 8 h, 12 h, 24 h and 32 h without replacement so as to avoid deviation from bacteria testing conditions. The measurements were done in triplicates. The amount of released LSZ was determined using a Bradford protein assay (Prod. No. P500-0006, Bio-Rad) [101]. The absorbance was measured at a wavelength of 595 nm (Xion 500, Dr. Lange GmbH). LSZ solutions with different concentrations were used as standard curves to extrapolate LSZ concentration.

The amount of released $Ca^{2+}$ in the supernatant was quantified using o-cresolphthalein complexone assay (Fluitest® Ca CPC, Analyticon, Germany). 2 ml of the assay reagent was added to 50 µl of supernatant and incubated for 15 min at room temperature. The absorbance was measured at 570 nm. The calcium concentration was calculated using standard curves (serial dilution of $CaCl_2$, 0-200 µg/ml). The

release tests followed the procedure of the optical density bacterial tests (see chapter 4.7).

### *4.7 In vivo assessment*

*In vivo* experiments to initially assess composite biocompatibility and resorption behaviour were carried out with four adult domestic female pigs. The study protocol was approved by the Local Animal Committee of the Government of Mid Franconia, Ansbach, Germany (approval no. 54-2531.31-25/07).

Three different composite types: protein-free composites, with 5 wt.% porcine serum albumin (PCA) and with 5 wt.% LSZ were tested. Porcine albumin was used instead of bovine serum albumin to limit any possible adverse reaction caused by proteins foreign to the test animal species. For LSZ no porcine derived products were commercially available, thus the LSZ from chicken egg white was used. Composites with cylindrical shape with dimensions of 14 mm in length and 10 mm in diameter and rounded off on one end were fabricated as previously described (section 2.2). Cylindrical scaffolds used for *in vivo* experiments are shown in Figure 4-1b (# symbol).

The surgical procedures were performed using intravenous anaesthesia and perioperative antibiosis, as described in [105, 106, 108]. To gain access to the frontal bone, an incision was made in the skin and the periosteum of the skull. Nine identical monocortical defects (10 mm diameter, 10 mm depth) were created in the frontal bone using a trephine burr (Roland Schmid, Fuerth, Germany). Cylindrical samples rounded off on one end and with dimensions of 14 mm in length and 10 mm in diameter (see Figure 4-1b, # symbol) were applied into the defects, such that the rounded ends protruded 4 mm above the defects and elevated the local periosteum. This periosteal elevation aimed to additionally generate bone above the samples [107, 116]. The periosteum and skin were sutured in 2 layers (Vicryl 3.0; Vicryl 1.0; Ethicon GmbH, KG, Norderstedt, Germany). According to the protocol each two animals were sacrificed after four and eight weeks post-operative and subsequently a multi-slice spiral CT examination (Somatom Plus 4 Volume Zoom, Siemens AG, Erlangen, Germany) with a slice thickness of 0.6 mm of the skull caps was performed. The specimens were subsequently prepared for microradiographic and light microscopic evaluation as described previously [105, 106, 108]. Obtained microradiographic images were analysed by Bioquant Osteo Software V 7.10.10 (Bioquant Image Analysis

Cooperation, Nashville, USA) to determine material persistence and new bone formation rates.

## *4.8. Bacterial tests*

### *4.8.1 Materials*

For the bacterial tests the gram-positive strains *Micrococcus luteus* (*M. luteus,* Cat. No. 20030, DSMZ) and *Listeria innocua* (*L. Innocua, Cat. No.* 20649) and the gram-negative strains *Escherichia coli* (1077, DSMZ) and *Pseudomonas fluorescens* (50090, DSMZ) were obtained from the Deutsche Sammlung von Mikroorganismen und Zellkulturen GmbH, Germany. The nutrients brain heart infusion (Prod. No. 53286, Fluka) and lysogeny broth (Prod. No. L3022, Sigma Aldrich) were obtained for bacteria cultivation. McFarland turbidity standard (Prod. No. R20421) was purchased from Remel, Germany).

### *4.8.2 Methods*

The antibacterial properties of the specimens were determined with three different assays: optical density measurements, total viability counts, and zone of inhibition tests (Kirby-Bauer tests [117]). The optical density measurements and total viability counts were done with two gram-positive (*M. luteus* and *L. innocua)* and two gram-negative (*E. coli* and *P. fluorescens*) bacteria strains. For the zone of inhibition tests only the *M. luteus* strain was used. Prior to the bacterial tests, all scaffolds were gamma-sterilised at a dosage of 25 kGy. These conditions were selected as used for commercial-scale sterilisation of medical supplies [118].

The bacteria were cultivated on agar and afterwards suspended in nutrient broth at a temperature of 20°C for 18 h. The agar plates were obtained by layering petri dishes with autoclaved, 60°C tempered agar medium enriched with 5 wt.% of nutrient. Brain heart infusion was used as nutrient for *M. luteus* and *L. innocua* whereas lysogeny broth was used for *E. coli* and *P. fluorescens*.

Bacteria were recollected by centrifugation at 2500 rpm for 10 min, dissolved in sterilised PBS and diluted to an optical density of 0.12. An optical density of 0.12 corresponds with a bacteria concentration of $3x10^8$ CFU/ml according to the McFarland turbidity standard. Cylindrical specimens (14 mm in diameter and 5.5 mm in height)

were immersed in 8 ml of the prepared bacteria stock solutions of the two different bacteria strains. For each scaffold type (with 0, 0.5, 1, 1.5, and 2.5 wt.% LSZ) five specimens were used and separately analysed. The optical density was measured by a plate reader (Plate CHAMELEON V, Hidex) using 0.2 ml of bacteria solution collected after 10 min, 30 min, 1 h, 2 h, 4 h, 8 h, 12 h, 24 h, and 32 h.

In addition LSZ control measurements were conducted by adding different amounts of LSZ to 8 ml bacteria stock solution resulting in two different LSZ concentrations (0.5 and 0.05 mg/ml). Throughout the experiments the testing tubes (Cat.-No. 525-0304, VWR) with the specimens and the bacteria solutions were kept at a constant temperature of 20 °C and shaken to avoid bacteria sedimentation.

For total viability counts bacteria supernatant was removed after 8 h and 24 h and diluted with PBS. As the bacteria concentration widely differed throughout the experiments for each measurement point several dilutions between 1 and 100000 were required to obtain reliable results. Optical density measurement results were used as reference points. The diluted bacteria suspension was uniformly spread with a Drigalski spatula on the agar plates and kept at 20 °C for three days. Afterwards the number of CFU was counted only considering plates with less than 300 colonies.

For the zone of inhibition tests three specimens of each sample type were imbedded in BHI-agar cooled down to 40 °C. This was necessary as the scaffolds were too heavy to be supported by the agar layer. Afterwards 0.33 ml of bacteria solution was dispersed on the prepared BHI-agar plates. After three days of cultivation time at 20 °C, samples were photographed to measure the size of the inhibition zone. All processing steps were done with sterilised media and under a clean bench to avoid any contamination.

# 5 Results

Chapter 5.1 was adapted from:

Mueller, B.; Zacharias, M.; Rezwan, K.; Bovine Serum Albumin and Lysozyme Adsorption on Calcium Phosphate Particles. Advanced Engineering Materials, 2010, Vol. 12, I. 1-2, p. B53-61 (license number 4119441141467).

Chapter 5.2 was adapted from:

Mueller, B.; Koch, D.; Lutz, R.; Schlegel, K. A.; Treccani, L.; Rezwan, K.; A novel one-pot process for near-net-shape fabrication of open-porous resorbable hydroxyapatite/protein composites and in vivo assessment. Materials Science and Engineering: C, 2014, Vol. 42, p. 137-145 (license number 4119440246729).

Chapter 5.3 was adapted from:

Mueller, B.; Treccani, L.; Rezwan, K.; Antibacterial active open-porous hydroxyapatite/lysozyme scaffolds suitable as bone graft and depot for localised drug delivery. Journal of Biomaterials Applications, Vol. 31, I. 8, p. 1123-1134

## 5.1 Protein adsorption on calcium phosphate

It is known, that on hydrophilic surfaces electrostatic interactions are one of the main factors for the adsorption of biomolecules on particle surfaces [41-46]. Therefore, in this study zeta potential measurements were chosen to characterise protein adsorption. In combination with VIS spectroscopy, the amount of protein adsorbed could be quantified. By this approach the protein adsorption potential of the powder could be defined.

### 5.1.1 Physical properties of calcium phosphate powders

Basic investigations on the physical properties of the calcium phosphate powders yielded the following results. The HAp powder has a particle size of 100 nm and a specific surface area of 58 m²/g. β-TCP powder has a particle size of 4.56 µm and a specific surface area of 1.4 m²/g. SEM pictures reveal that the HAp particles are prismatic with an aspect ratio of 4 whereas the β-TCP particles are spherical (Table 5-1).

**Table 5-1. Physical properties of calcium phosphates as measured**

| | HAp | β-TCP |
|---|---|---|
| Crystal structure | hexagonal | trigonal |
| Theoretical density [g/cm³] | 3.15 | 3.10 |
| Measured density [g/cm³] | 3.185 ± 0,009 | 3.117 ± 0,012 |
| Particle aspect ratio | 4 | 1 |
| Particle size distribution [µm] ($d_{50}$ ± peak width) | 0.10 ± 0.27 | 4.56 ± 0.44 |
| Specific surface area [m²/g] | 58.23 ± 0,11 | 1.38 ± 0,04 |
| IEP at pH (heat-treated at 200°C) | 6.8 | 6.2 |

In Figure 5-1 $Ca^{2+}$-solubility of the two calcium phosphate powders was measured as a function of pH. The $Ca^{2+}$-solubility curves of HAp and β-TCP show a similar increase at a pH value below 6. At a pH value above 6 the $Ca^{2+}$-solubility of β-TCP is higher than of HAp. The specific pH values at which protein adsorption experiments were carried out are marked as a dashed line for both powders. The adsorption pH was not pre-adjusted to a certain pH by titration but the equilibrium pH of the respective powder suspensions was taken. The adsorption pH for HAp powder is at 7.0 ± 0.1 and for β-TCP powder at 8.1 ± 0.1. At adsorption pH the $Ca^{2+}$-solubility of HAp is higher than of β-TCP although β-TCP solubility is higher as compared to HAp at neutral and basic pH. Standard deviations were determined but amounting to 1-2 % they are too small to be seen in the graphs at logarithmic scaling.

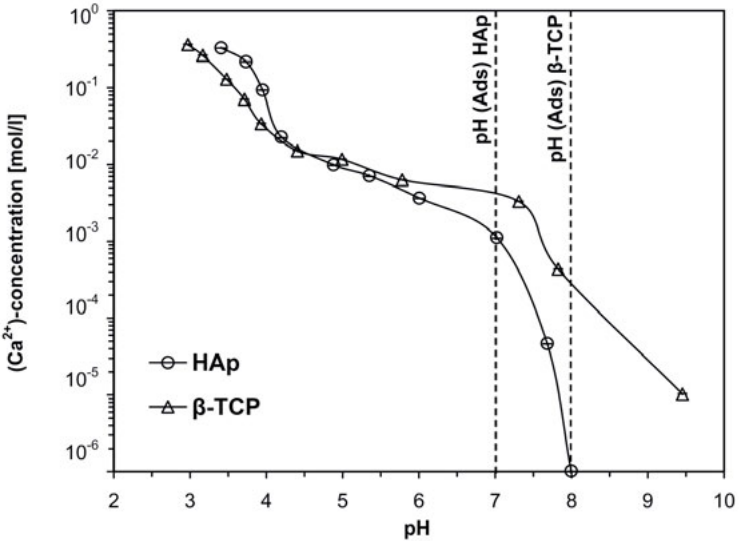


**Figure 5-1. ($Ca^{2+}$)-solubility of calcium phosphate powders as a function of pH after an equilibration time of 72 hrs. The different pHs of adsorption are marked by the dashed lines, HAp shows an increased solubility at adsorption pH 7 as compared to β-TCP at 8. Standard deviations were determined within 1 to 2 % but are too small to be seen at the logarithmic scaling.**

### *5.1.2 Combined zeta potential / VIS spectroscopy measurements*

Figure 5-2 shows the zeta potential and conductivity curves against pH for HAp powder without and with addition of different amounts of BSA (a) and LSZ (b). The corresponding curves for β-TCP powder are given in Figure 5-3. The starting point of the experiments is marked by a dashed line and the arrows indicate the two titration directions. In all cases the measurements were started at corresponding equilibrium pH values after 16 hrs. The influence of the protein addition as compared to the equilibrium pH is minimal (±0.2), except for LSZ addition to HAp suspensions where a clear drift is noticeable. With increasing LSZ content the equilibrium pH changes from 7.0 to 6.1 at the highest protein addition. The starting electrical conductivity of both suspensions is at the same level, indicating a comparable initial ionic strength (corresponding to approx. 3.3 mM KCl at 25 °C [119]) within the detection limits. The electrical conductivity of the powder suspensions does hardly change with increasing

protein content. Only for HAp and LSZ an increase in conductivity from 0.05 to 0.1 S/m with increasing LSZ addition was observed.

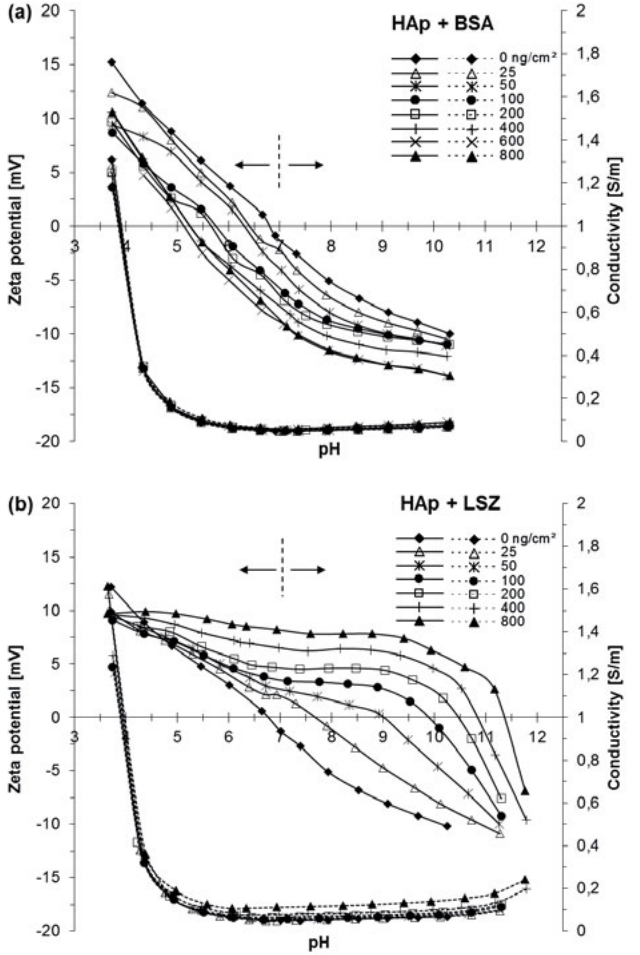


**Figure 5-2. Zeta potential (solid) and conductivity (dashed) curves of 1 Vol% HAp powder suspensions without (0 ng/cm²) and with different additions of BSA (a) and LSZ (b), measured after 16 hrs of adsorption time at the initial pH of 7 and beginning at adsorption pH. An independent acidic and alkaline titration was conducted for each suspension (indicated by the arrows) and joined as one curve. Protein additions are normalized to the powder surface area.**

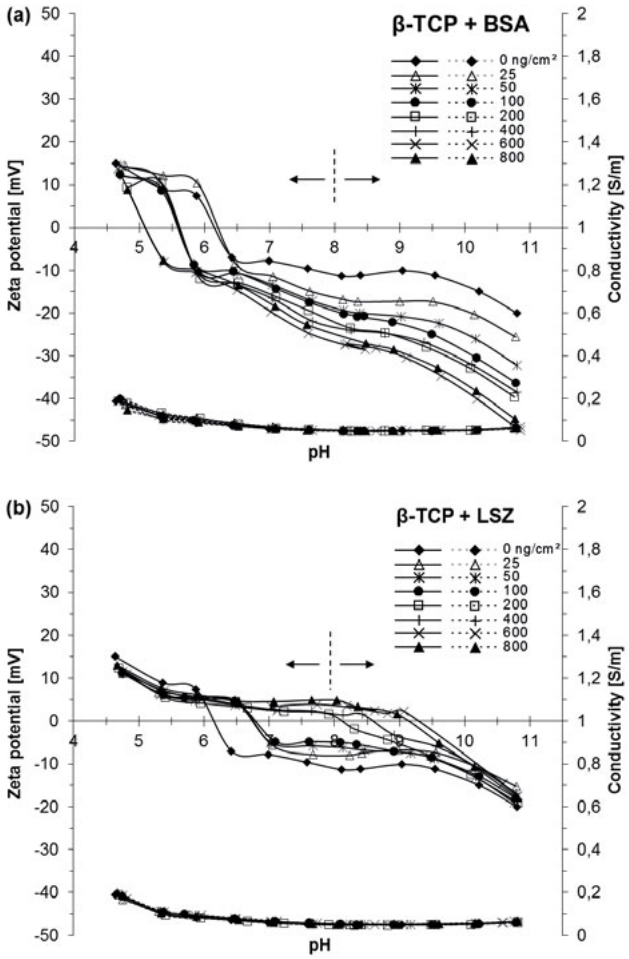


**Figure 5-3. Zeta potential (solid) and conductivity (dashed) curves of 1 Vol% β-TCP powder suspensions without (0 ng/cm²) and with different additions of BSA (a) and LSZ (b), measured after 16 hrs of adsorption time at pH 8 and beginning at adsorption pH. An independent acidic and alkaline titration was conducted for each suspension (indicated by the arrows) and joined as one curve. Protein additions are normalized to the powder surface area.**

The zeta potential measurements of the calcium phosphates without protein addition resulted in an IEP at pH 6.8 for the investigated HAp powder and 6.2 for the

β-TCP powder. With increasing protein content in the suspensions the IEPs of the calcium phosphate powders were shifted, with BSA addition towards acidic pH and with LSZ addition towards alkaline pH. For most of the samples there was no further change in IEP observed once a certain protein addition was reached. For BSA this point is reached at pH 5.1-5.2 for both calcium phosphate powders, for HAp at an added protein amount of 400 ng/cm² and for β-TCP at 600 ng/cm². In the case of LSZ no such point is reached for HAp. For the highest LSZ addition (800 ng/cm²) the IEP is at pH 11.3. The β-TCP powder reaches the point of no further change of IEP at 600 ng/cm² at a pH of 9.3. The initial zeta potential for both powders is low and moves between +15 and -15 mV in the measured pH range. The zeta potential does not increase with protein addition except for β-TCP and BSA. Here the zeta potential increases at alkaline pH to almost -50 mV for high BSA additions (see Figure 5-3a).

Figure 5-4 a and b shows the results of the VIS spectroscopy measurements for BSA and LSZ adsorption on the calcium phosphate powders. The x-axis shows the amount of added protein to the suspension whereas the y-axis shows the amount of protein that adsorbed after 16 hrs. In none of the experiments the protein adsorption exceeded 200 ng/cm². On HAp 104 ng/cm² of BSA and 78 ng/cm² of LSZ were adsorbed. On β-TCP the amount of adsorbed protein was higher with values of 162 ng/cm² for BSA and 171 ng/cm² for LSZ. The theoretical end-on and side-on adsorption values, indicated by the dotted lines in Fig. 4 a and b, were calculated from the molecular weight and dimensions of the proteins (summarized in Table 4-1) by assuming regular monolayer configuration [120] and treating the proteins as hard particles, disregarding electrostatic interactions. The BSA adsorption curves show a similar progress for both powders. At low protein additions up to 100 ng/cm² almost all added BSA was adsorbed. At higher BSA additions the amount of adsorbed protein is not increasing for HAp or shows only a comparably low increase in the case of β-TCP. Beginning at an initial protein concentration of 600 ng/cm², BSA adsorption is higher on β-TCP than on HAp. In contrast, the LSZ adsorption curves show a more distinct difference. Only at low initial protein concentrations up to 50 ng/cm² the measured values are on the same level. At higher initial concentrations, more LSZ was adsorbed on β-TCP than on HAp. Generally the LSZ adsorption curves show a more continuous increase from low to high protein additions as compared to BSA.

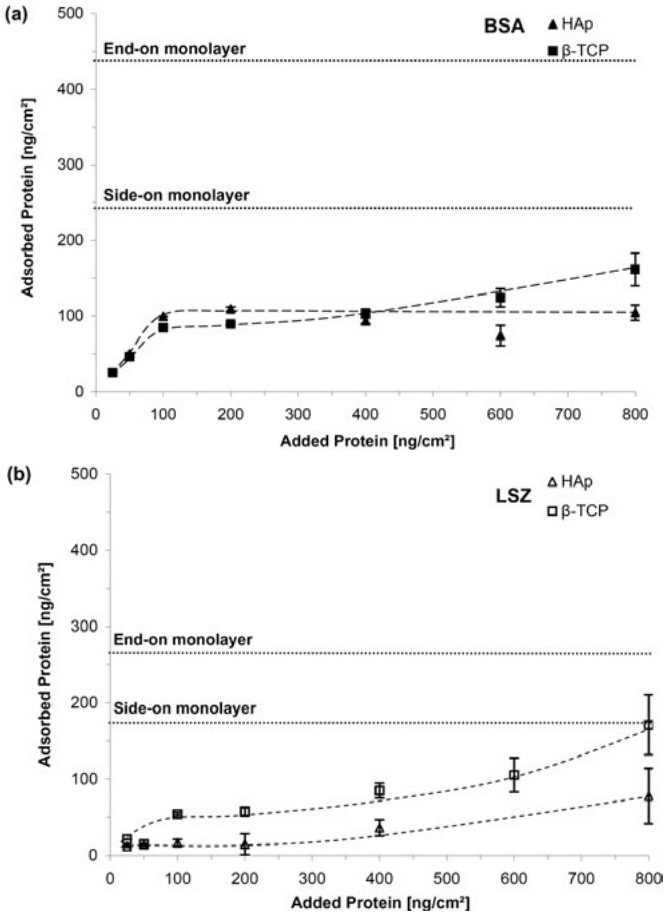


**Figure 5-4. BSA (a) and LSZ (b) adsorption curves for the calcium phosphate powders after 16 hrs of adsorption time. Theoretical end-on and side-on monolayers, calculated from the protein data (regular adsorption type, see Fig. 7 for further explanation), are indicated by the dotted lines. A regular side-on monolayer could only be achieved in the case of LSZ and β-TCP (b). Measured by VIS spectroscopy and normalised to powder surface area.**

Figure 5-5 shows the percentage of adsorbed protein relative to the total amount of added protein. The relative BSA adsorption is high at low protein additions up to 100 ng/cm² reaching values of over 85 % and strongly decreasing at higher initial concentrations. For LSZ the percentage of adsorption is at a lower level at minor

protein additions (most values less than 55 %) and is decreasing continuously. At protein additions ranging between 200 ng/cm² (HAp) and 400 ng/cm² (β-TCP) a plateau value of ± 2 % is reached for LSZ. For BSA adsorption a plateau value is reached at 600 ng/cm² for both powders.

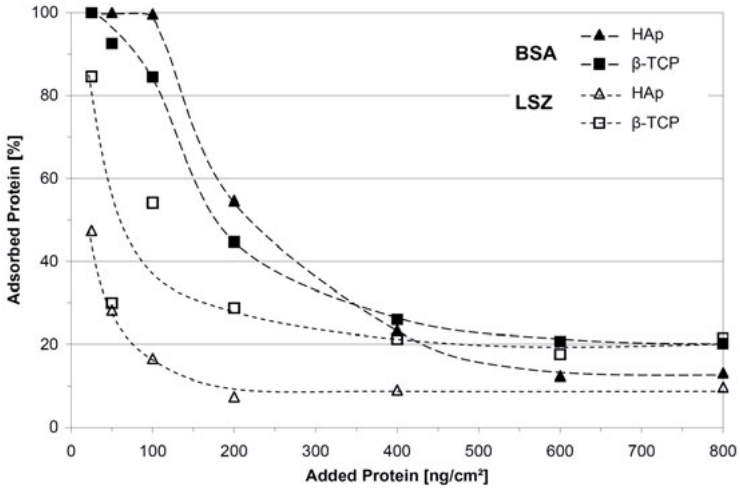


**Figure 5-5. Relative protein adsorption amount plotted as a function of added protein to the powder suspensions. An adsorption plateau between the protein in suspension and the adsorbed protein on the surface is developing with increasing protein addition. For BSA it is reached at 600 ng/cm², for LSZ at only 200 to 400 ng/cm².**

Figure 5-6 combines the zeta potential and VIS spectroscopy results. The amount of adsorbed protein is plotted against zeta potential at the corresponding adsorption pH. Adsorbed BSA leads to a negative zeta potential whereas adsorbed LSZ leads to a positive zeta potential. A zeta potential plateau within ±1 mV for BSA is reached at an adsorption of 74 ng/cm² on HAp and 124 ng/cm² on β-TCP powder. In the case of LSZ an adsorbed amount of 36 ng/cm² for HAp and 105 ng/cm² for β-TCP is required to reach a zeta potential plateau.

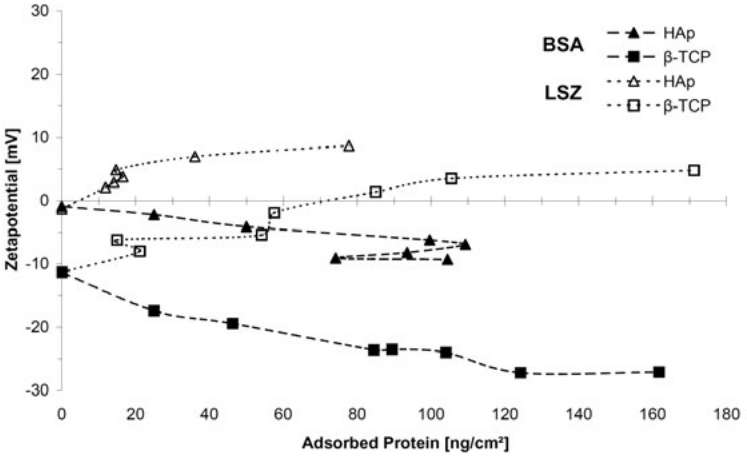


**Figure 5-6. Zeta potential plotted as a function of adsorbed protein after 16 hrs of adsorption time at equilibrium pH of the specific suspensions (for HAp at pH 7 and for β-TCP at pH 8 respectively). A negative zeta potential is developing with the addition of negatively charged BSA whereas the zeta potential moves towards more positive values with the addition of positively charged LSZ.**

## *5.2 Fabrication and characterisation of Hydroxyapatite/Protein Scaffolds*

The freeze gelation process was applied to fabricate biocompatible, near-net, complex-shaped hydroxyapatite/protein composites. Protein was directly integrated during scaffold processing. Two model proteins, BSA and LSZ, featuring different and well-known properties and present in high amount in body fluids were selected. The effect of the two model proteins, BSA and LSZ, on final scaffold microstructure and mechanical stability was investigated by electron microscopy, mercury intrusion porosimetry, and by biaxial strength tests. Composite degradation behaviour and protein release was assessed by in vitro studies at different storage times and storage conditions. Moreover, a first in vivo assessment of the biocompatibility and resorption behaviour of hydroxyapatite/protein composites in a pig model is reported.

### *5.2.1 Fabrication process and composite structure*

Porous HAp/protein composites were prepared via the one-pot-process mixing HAp, silica sol and two different blood serum proteins (BSA and LSZ) at different percentage (1 wt.% and 5 wt.%, respectively). After freezing at -150°C, the samples were demoulded and dried at room temperature, at different r.h. and for different time periods. Even after demoulding the composites in a green body state featured good properties with respect to handling. Some representative images of HAp/protein composites featuring different shapes and sizes are given in Figure 4-1. Composites with different near-net shapes were obtained using different mould geometries, whilst fabrication parameters were unvaried.

The microstructures of protein-free, HAp/BSA-5 and HAp/LSZ-5 are representatively given in Figure 5-7. SEM image analysis revealed the presence of micrometer-sized pores for BSA-containing composites. HAp/BSA-5 presented pores with ~100 µm (Figure 5-7b), whereas HAp/BSA-1 had smaller pores of ~73 µm (data not shown). On HAp/LSZ composites few pores with sizes up to ~5 µm could be observed (Figure 5-7c). No visible pores were observed on protein-free composites (Figure 5-7a).

**Table 5-2. Pore size distribution and porosity of the composites (as measured by mercury intrusion porosimetry*, calculated from the discs' weight and dimensions+, and evaluated by SEM images#)**

| Composite type | Average pore diameter | | Open porosity* [%] | Total porosity+ [%] | Ratio open/total porosity |
|---|---|---|---|---|---|
| | Peak 1* [nm] | Peak 2# [µm] | | | |
| protein-free | 35 | - | 51.00 | 56.16 ± 1.69 | 0.91 |
| HAp/BSA-1 | 36 | 73 ± 27 | 55.19 | 65.69 ± 1.90 | 0.84 |
| HAp/BSA-5 | 57 | 100 ± 29 | 56.30 | 66.74 ± 1.42 | 0.84 |
| HAp/LSZ-1 | 33 | - | 48.93 | 56.02 ± 1.42 | 0.87 |
| HAp/LSZ-5 | 28 | - | 40.41 | 50.39 ± 1.42 | 0.80 |

The mercury intrusion porosimetry performed on all composite types revealed the presence of open pores in nanometer-range (28 - 57 nm). The pore size and porosity values as well as the ratio open/total porosity for each composite are summarised in Table 5-2. Protein-free and HAp/LSZ composites had a lower open porosity than

HAp/BSA composites, ~51 % and a total porosity of ~56 %, respectively. The highest open (~56 %) and total porosity (~67. %) was measured for HAp/BSA-5 composites. The lowest open (~40 %) and total porosity (~50. %) was measured for HAp/LSZ-5 composites. HAp/protein composites had a lower open/total porosity ratio than protein-free composites, the lowest ratio of 0.80 having been measured for HAp/LSZ-5.

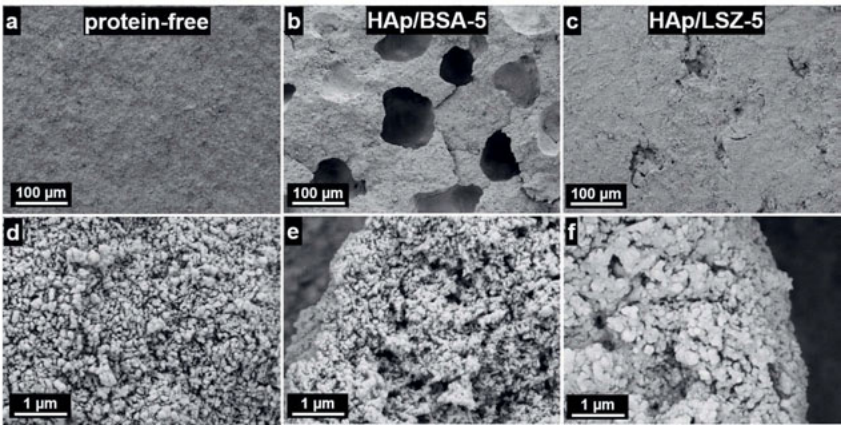


**Figure 5-7. SEM micrographs of composites without protein (a, d), with 5 wt.% BSA (b, e), and with 5 wt.% LSZ (c, f) at two magnifications. Without protein the average pore size of the interconnected pores is 35 nm. For BSA-containing composites pores up to 100 µm are generated due to a foaming effect during slurry preparation initiated at high stirring velocities. For composites containing LSZ the largest pores reach 5 µm.**

### *5.2.2. Mechanical strength*

The influence of storage time and conditions on the mechanical behaviour of the composites was examined by measuring the biaxial flexure strength after 1, 3, 6, 9, and 12 weeks storage. The effect of storage at two different humidity conditions of 97 % and 30 % r. h. was observed beginning at week 2. Up to 1 week all composites were slowly dried at relative high humidity (97 % r. h) to reduce crack formation and increase sample stability. Figure 5-8 shows the results of the biaxial flexure strength test of the composites as a function of storage time, whereas Figure 5-9 shows the achieved maximum strength values against the composites' total porosity. The biaxial strength

values of composites stored for 1 week were plotted in all graphs as initial composite strength.

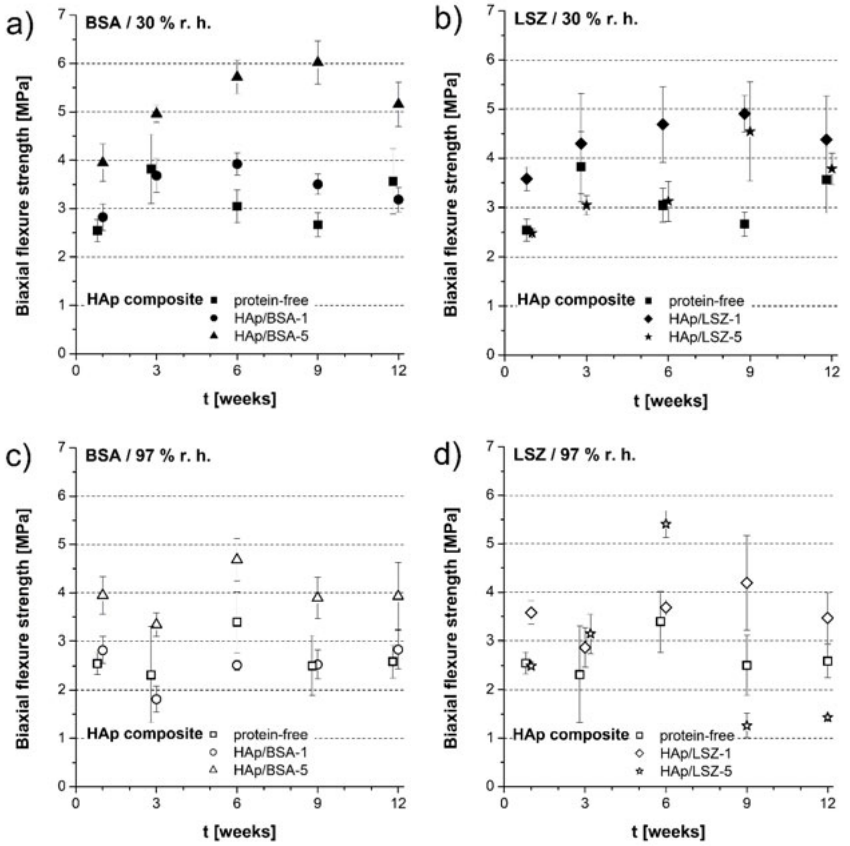


**Figure 5-8. Biaxial flexure strength of composites with 0, 1 and 5 wt.% of BSA (a, c) and LSZ (b, d). The HAp/protein composites were stored at room temperature and relative humidities of 30 % (a, b) and 97 % (c, d), respectively. Measurements were taken after 1, 3, 6, 9, and 12 weeks. The highest strength was attained for 5 wt.% of BSA after 9 weeks of storage time.**

All produced composite samples allowed very good handling both for mechanical and *in vivo* testing. The strength of the reference material without protein was 2.9 ± 0.5 MPa in average, independent of storage time and relative humidity. By protein addition the strength of the HAp composites could be enhanced for most compositions, with

BSA integration resulting in a higher maximum mechanical stability than LSZ integration. The highest strength measured for BSA containing composites was 6 ± 0.4 MPa whereas it was 5.4 ± 0.3 MPa for LSZ containing composites. The strongest BSA containing composites featured a total porosity of 65.5 ± 0.1 % whereas the strongest LSZ containing composites had a porosity of only 49.1 ± 0.1 % (Figure 5-9). Both peak strength values were detected for composites with 5 wt.% of protein. For BSA-containing composites higher protein content led to higher strength as HAp/BSA-1 composites had only a strength of 3.0 ± 0.5 MPa in average. For LSZ-containing composites only at 97 % r. h. and 6 weeks a higher strength value was measured for composites with 5 wt.% protein than for composites with 1 wt.%. In all other cases the strength of HAp/LSZ-5 composites was on the same level or lower than for HAp/LSZ-1 composites.

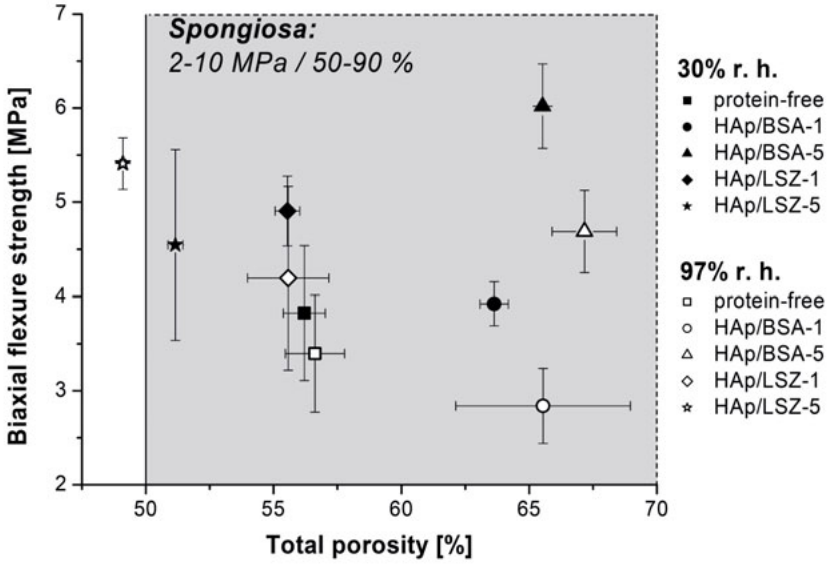


**Figure 5-9. Strength maxima of composites without protein, with 1 and 5 wt.% of BSA, and with 1 and 5 wt.% of LSZ stored at different relative humidity plotted against total porosity of the composites. Despite the high porosity of 65.5 % the highest strength value of 6.0 ± 0.4 MPa was measured for HAp/BSA-5 composites stored at 30 % r. h.**

**Except for HAp/LSZ-5 composites all composites show the highest strength at a relative humidity of 30 %. To draw the comparison to human *spongiosa* its flexural strength and porosity range are indicated in the diagram [57, 58, 121]. All values except for one (HAp/LSZ-5 at 97 % r. h.) are in the range of the human *spongiosa*.**

With storage time the strength of the protein-containing composites generally increased with maximum peaks after 6 or 9 weeks followed by a slight strength decrease over time. Only for HAp/LSZ-5 composites at 97 % r. h. the strength decreased massively to 1.3 ± 0.3 MPa with 9 weeks storage time. The storage at 30 % r. h. resulted in general in stronger composites than storage at 97 % r. h. (Figure 5-9). Furthermore the strength increase over storage time was in most cases more distinctive at 30 % r. h. The human *spongiosa* flexural strength of both wet and dry spongiosa samples ranges from 2-10 MPa whereas the total porosity varies from 50 to 90 % [57, 58, 121]. As a guiding reference these literature values are highlighted in Figure 5-9 (grey shadowed area).

### *5.2.3 Protein release*

Protein release at different times was characterised in order to assess the potential of the fabricated scaffolds for controlled drug release. The results of the protein release experiments are shown in Figure 5-10. The protein release was measured for 1, 3, 6, 9, and 12 week old samples and normalised to the initial protein content of each sample. All composite types showed a similar release behaviour for both storage humidities at 30 % and 97 % r. h. For all cases, except HAp/LSZ-5 composites, protein release was decreasing with increasing storage time. Composites with BSA released a higher total protein amount than composites with LSZ. Furthermore, composites containing 5 wt.% of protein released a higher percentage of protein than composites containing 1 wt.% of protein. From 1 to 9 weeks of storage time up to 80% of initial proteins present in the sample were released. After 12 weeks the protein release was decreasing to 76 ± 2 % (30 % r. h.) and 66 ± 6 % (97 % r. h.), respectively. HAp/LSZ-1 composites showed the lowest protein release of 20 ± 6 % (97 % r. h.) at 12 weeks. HAp/LSZ-5 composites showed increasing protein release over storage time at 97 % r. h. For 30 % r. h. the release was overall decreasing but with a very inconsistent progression showing the lowest release value at 6 weeks of storage time.

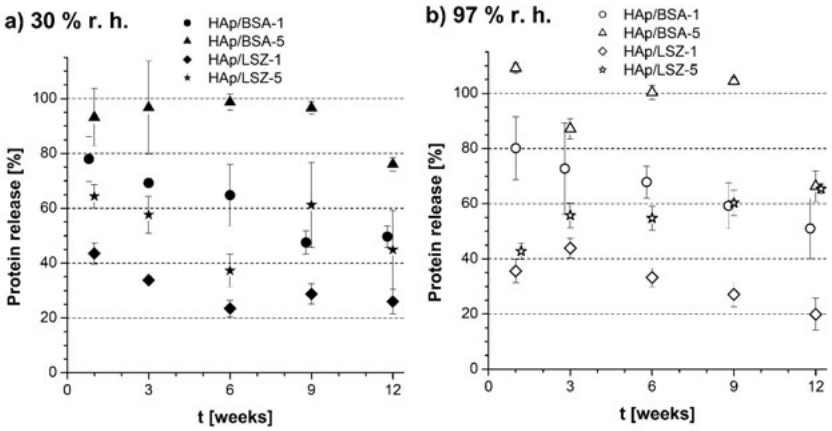


**Figure 5-10. Protein release of HAp/protein composites as compared to initial protein content of the samples. The composites were stored in PBS buffer solution at 37°C under static experimental conditions. Measurements were done after composite storage periods of 1, 3, 6, 9, and 12 weeks at a relative humidity of 30 % (a) and 97 % (b). With increasing storage time the protein release of the composites decreased except for HAp/LSZ-5. The protein release is not significantly influenced by different relative humidity.**

### *5.2.4 In vivo assessment*

*In vivo* the samples showed ongoing resorption of the HAp specimens between 4 and 8 weeks. After 4 weeks 62.4 ± 16.1 % of the material were persistent in the LSZ group and 58.7 ± 16.1 % in the group without protein, while the group with albumin showed a material persistence of 50.4 ± 4.3 %. Eight weeks post-operative the groups with albumin and without protein showed a material persistence of 35.0 ± 2.1 % and 35.4 ± 1.5 %, respectively. The LSZ group, where 48.3 ± 17 % of the material were not resorbed, showed the highest persistence. In this group also fewer specimens showed osteoconductive properties compared to the other groups. New bone formation was visible in all tested groups. After 4 weeks the group without protein showed a new bone formation rate of 14.3 ± 10.3 %, the LSZ group 10.1 ± 5.3 % and the albumin group 14.2 ± 2.3 %. After 8 weeks the highest bone formation rate was found for the albumin group (36.9 ± 3.0 %) compared to the group without protein (31.2 ± 2.8%) and the LSZ group (20.6 ± 9.1%). The groups without protein and with albumin showed

considerable bone regeneration rates of 31.2 ± 2.8 % and 36.9 ± 3.0 %, respectively. The LSZ group showed bone regeneration of 20.6 ± 9.1%. This lower bone regeneration rate might be explained by the applied chicken LSZ being foreign to the test animal species. However it was noticeable, that there was a great interindividual difference regarding material degeneration and bone regeneration between the animals after 8 weeks. While one animal showed complete regeneration, even above the margin of the defects (Figure 5-11a), the other animal showed a higher rate of material persistence and lower bone formation (Figure 5-11b). Nevertheless the intended effect of bone formation above the sample through periosteal elevation is visible in this animal (Figure 5-11b). Osteoconductive properties were found for the material remaining in the defect (Figure 5-11c). The remaining HAp specimens are marked by black asterisks. Along the HAp material newly formed bone is visible, which has grown on the specimen's surface. In the histological staining (Toluidine blue O) the newly formed bone appears purple and the osteoid appears blue.

This osteoconductive effect is also visible in the samples cracks, which are visible in the computed tomography (Figure 5-11b). Thus the cracking of the samples had no negative influence on bone regeneration in this non load bearing setting, but allowed accelerated regeneration of the defects along the cracks, similar as observed for granulate materials [106].

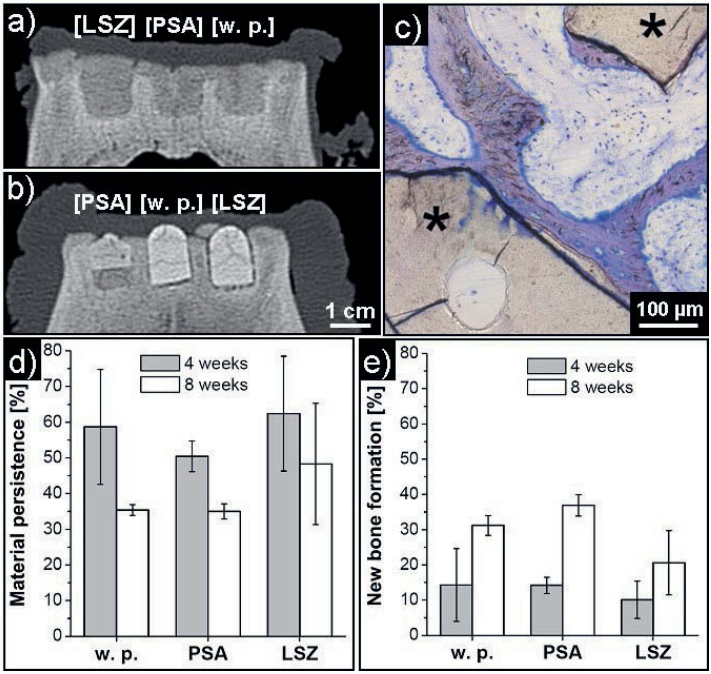


**Figure 5-11. Computer Tomography micrographs (a, b), microscopy image (c), material persistence (d) and newly formed bone rate (e) of *in vivo* samples after 8 weeks. One animal (a) showed complete resorption and bone reconstruction for composites without protein (w. p.), with 5 wt.% chicken egg white lysozyme (LSZ), and 5 wt.% porcine serum albumin (PSA). Another animal (b) showed beginning resorption of the PSA composite and no resorption for the other composite types. Osteoconductive properties were found for the material remaining in the defects (c). Remaining material of the HAp specimens (without protein) is marked by black asterisks. The newly formed bone appears purple and the osteoid appears blue (Toluidine blue O staining).**

## *5.3 Functionalisation of scaffolds with active biomolecules*

To demonstrate that the freeze gelation process is suitable for the integration of biological compounds into an ceramic matrix [96] lysozyme (LSZ) was used as a model macromolecular drug. LSZ destroys gram-positive bacteria by damaging their cell walls and its activity can be clearly tested by microbiological tests. HAp scaffolds containing 0.5, 1.0, 1.5 and 2.5 wt.% LSZ and without LSZ were fabricated by freeze gelation. The scaffolds were characterised in terms of porosity, mechanical strength, protein release and antibacterial effect to demonstrate their suitability as bone replacement material and drug delivery system.

### *5.3.1 Scaffold characterisation*

For this part of the study HAp/LSZ scaffolds with 0.5, 1.0, 1.5, and 2.5 wt.% LSZ were fabricated. Biaxial flexure strength vs. total porosity is plotted in Figure 5-12a. SEM images of polished sections of the scaffolds are given in Figure 5-12b. The biaxial flexure strength was varying between 1.7 ± 0.1 MPa (with 0.5 wt.% LSZ) and 5 ± 0.6 MPa (2.5 wt.% LSZ). Likewise the total porosity was varying between 63 ± 0.6 % (0.5 wt.% LSZ) and 55.4 ± 1.3 % (2.5 wt.% LSZ). Scaffolds without LSZ had a strength of 3.6 ± 0.7 MPa and a porosity of 56.5 ± 0.9 %. All scaffolds had an average nano-pore size of around 50 nm measured by mercury intrusion porosimetry. SEM images (Figure 5-12b) revealed larger micropores with lamellar morphology up to 100 µm in length in scaffolds with 0.5 and 1.0 wt.% LSZ which moreover showed an alignment. In contrast in scaffolds with 0.0, 1.5, and 2.5 wt.% pores had a size up to 5 µm and cellular morphology. According to mercury intrusion porosimetry measurements over 90 % of the total pore volume was interconnected.

The water evaporation during the drying period led to a shrinkage of 25 ± 1 % for scaffolds with 0.0, 1.5, and 2.5 wt.% LSZ. The scaffolds with larger pores (1.0 and 0.5 wt.% LSZ) had a shrinkage of 21 and 15 %, respectively.

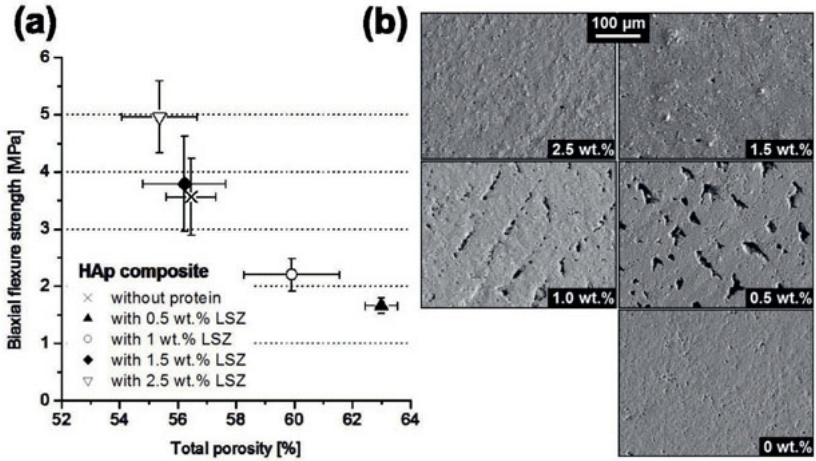


**Figure 5-12. (a) Incorporation of LSZ into HAp scaffolds influences their mechanical strength. Scaffolds with 2.5 wt.% LSZ showed an increased biaxial flexure strength of 5.0 ± 0.6 MPa as compared to protein-free scaffolds with 3.6±0.7 MPa. For scaffolds with 0.5 and 1.0 wt.% of LSZ a reduced flexure strength compared to protein-free scaffolds was found. The mechanical strength of the scaffolds is strongly influenced by their differing total porosity. (b) SEM images of the scaffolds with 0.5 and 2.5 wt.% are given to illustrate the different textures.**

The behaviour of the dried scaffold in contact with liquids, the release of calcium ions and LSZ molecules loaded in the scaffold, was considered up to 32 h. When immersed in liquid the dried scaffolds remained intact. As shown in Figure 5-13, two main LSZ release pattern can be identified as a function of the incorporate LSZ. The amount of LSZ is expressed in mg/ml to correlate with the amount of LSZ used for bacterial tests. The highest LSZ release was observed after 32 h for scaffolds with 1.5 wt.% and 2.5 wt.% LSZ and the highest LSZ concentration released was ~ 0.40 mg/ml. The concentration of LSZ released correspond to ~ 15 % and ~ 8% of the initial quantity of protein introduced in 1.5 wt.% LSZ and 2.5 wt.% LSZ scaffolds, respectively. A lower LSZ release (~ 0.05 mg/ml after 32 h) was observed for scaffolds with 0.5 and 1.0 wt.% LSZ corresponding to 3.9 and 3.8 % of the initial LSZ content, respectively.

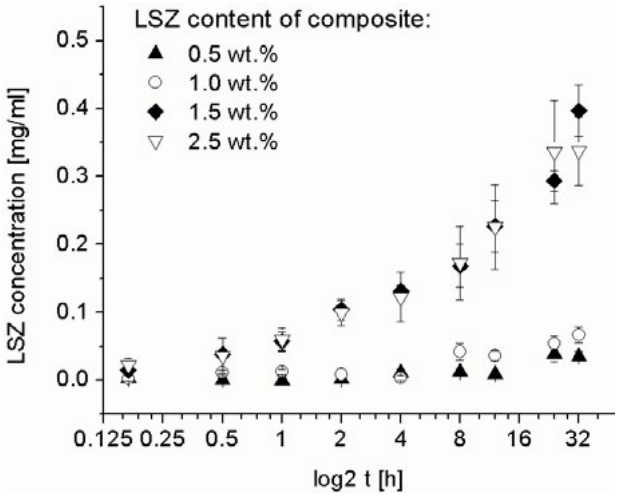


**Figure 5-13. LSZ release of HAp scaffolds with 0.5, 1, 1.5, and 2.5 wt.% LSZ in PBS solution over a period of 32 h determined by VIS spectroscopy.**

Figure 5-14 shows the $Ca^{2+}$ release under experimental conditions in PBS. $Ca^{2+}$ release amounts lower than $10^{-4}$ M were found. Until 24 h no $Ca^{2+}$ could be measured as all results were under the detection limit of 0.05 mmol/l of the applied test method. For scaffolds with 0.5 wt.% LSZ all values were under the detection limit. For comparison $Ca^{2+}$ release was also observed in demineralised water leading to ten-times higher values.

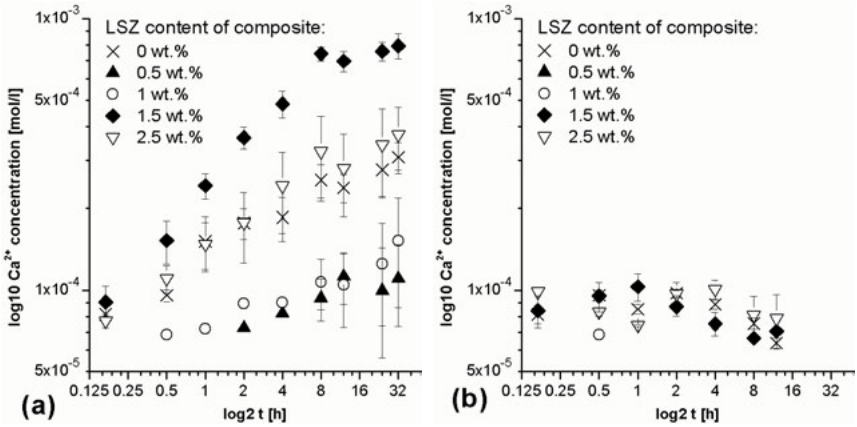


**Figure 5-14. $Ca^{2+}$ release of HAp scaffolds with 0, 0.5, 1, 1.5, and 2.5 wt.% LSZ over a 32-hour-time-period as determined by VIS spectroscopy (a) in demineralised water and (b) in PBS. In demineralised water the $Ca^{2+}$ release reaches a plateau value at 8 h for all scaffold types. Under experimental conditions in PBS the $Ca^{2+}$ release is on average ten times lower.**

### *5.3.2 Bacterial tests*

The antibacterial efficacy of the HAp/LSZ scaffolds and released LSZ against both gram-positive bacteria *M. luteus* and *L. innocua* were evaluated in vitro during a period of 32 h using different assays.

The activity of LSZ released from scaffolds embedded into agar plates was monitored with *M. luteus* by means of a zone of inhibition test, also called a Kirby-Bauer test. This test is used clinically to determine the ability of antimicrobial agents to inhibit microbial growth. If the bacterial strain is susceptible to the antimicrobial agent, a clear zone (the zone of inhibition) appears on the agar plate around the specimen. The formation of inhibition on the agar plates was observed around all HAp/LSZ scaffolds but not around the scaffolds without protein. Some representative images taken after 3 days cultivation (Figure 5-15a-e) show that the extension of the inhibition zone is proportional to the amount of LSZ loaded in the scaffold (Figure 5-15f). The largest inhibition was observed for scaffolds containing 2.5 wt.% LSZ.

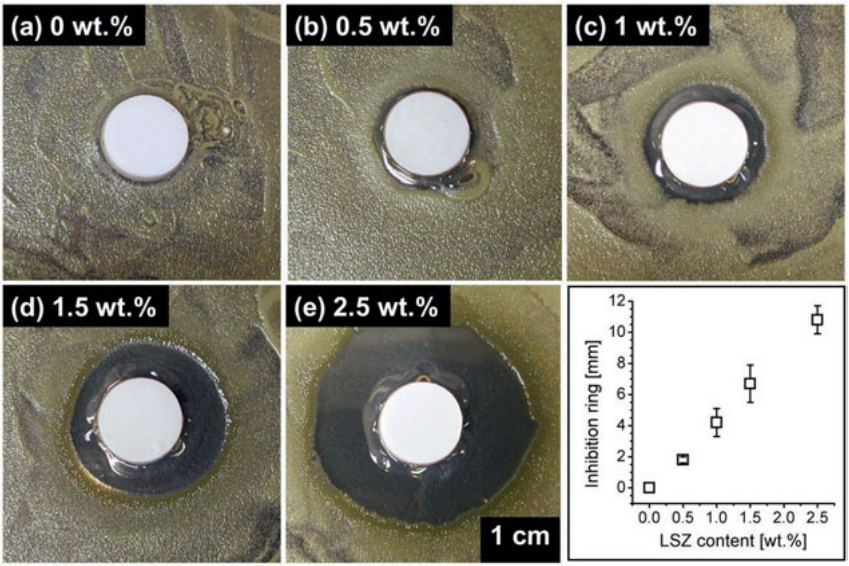


**Figure 5-15. Qualitative analysis of the antibacterial effect of HAp/LSZ scaffolds on gram-positive bacteria. Agar plates with embedded scaffolds were cultivated for 3 days with $10^8$ *M. luteus* bacteria cells each. For LSZ containing scaffolds an inhibition zone around the specimens is developed (b-e). The size of the inhibition zone increases with increasing LSZ content of the embedded scaffolds. The average inhibition zone size is given in (f).**

The antibacterial activity of LSZ released from the HAp/LSZ scaffolds was measured with *M. luteus* and *L. innocua* by means of turbidimetric and total viability tests (Figure 5-16). The bacteria stock solutions (initial bacteria concentration of 3 x $10^8$ CFU/ml) and LSZ-free scaffolds were used as a reference.

The bacteria concentration in the stock solution was screened by total viability counts after 8 h and 24 h. For *L. innocua* both at 8 and 24 h counts results close to the initial bacteria number in stock solution of 3 x $10^8$ CFU/ml were found.

For *M. luteus* the bacteria number in stock solution was also constant over the observed time period however counts yielded only 0.8 x $10^8$ CFU/ml after 8 h and 24 h which is presumably due to the comparatively longer growth period of *M. luteus* as compared to *L. innocua*. Therefore fewer *M. luteus* colonies become visible.

A die back of *M. luteus* and a growth inhibition for *L. innocua* in contact with HAp/LSZ scaffolds were observed during a time period of 32 h. Scaffold with 2.5 wt.% LSZ showed the highest antibacterial activity and an optical density corresponding to 0 CFU/ml was measured already after 30 min. For scaffolds with 0.5 wt.% LSZ the decline in bacteria concentration was slower. The OD after 32 h corresponded to 0.19 x $10^8$ CFU/ml denoting that only 0.006 % of added bacteria were still alive (Figure 5-16a). The total viability count test confirmed these results (Figure 5-16b). After 8 h viable *M. luteus* bacteria could only be detected for scaffolds with 0.5 wt.% LSZ, but after 24 h no viable bacteria were observed for any LSZ containing scaffolds. The scaffolds without LSZ showed bacteria numbers after 8 and 24 h of 1.4 and 0.6 x $10^8$ CFU/ml, respectively and an increased optical density as compared to the stock solution was observed beginning at 2 h.

For *L. innocua* the optical density remained constant for all samples up to 4 h and after 8 h a slight increase in optical density can be observed for all samples (Figure 5-16c). The total viability counts revealed an almost equal bacteria number for all samples. Measurements after 8 and 24 h yielded similar results for all scaffold types (Figure 5-16d).

*E.coli* and *P. fluorescens* showed constant bacteria concentration up to 4h. Subsequently strong bacteria proliferation both in contact with LSZ-free and LSZ-containing scaffolds was observed (data not shown).

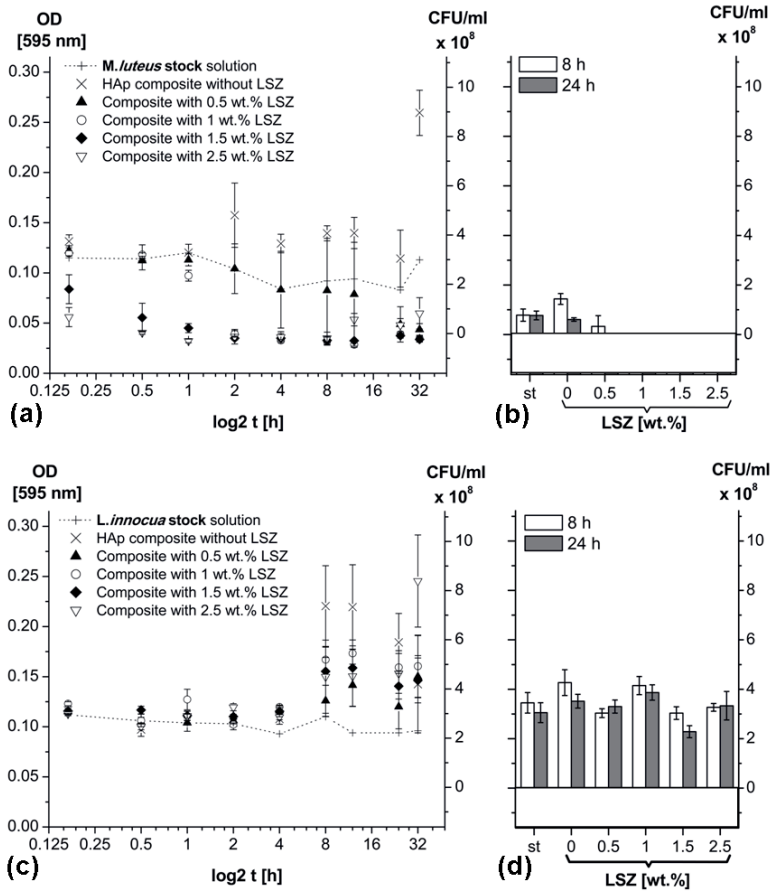


**Figure 5-16. Proliferation of gram-positive bacteria in the presence of HAp/LSZ scaffolds determined by optical density measurements over a period of 32 h (a, c) and by total viability counts after 8 and 24 h (b, d). The experiments were carried out for the bacteria stock solutions (st) and for scaffolds with 0, 0.5, 1, 1.5, and 2.5 wt.% LSZ. The dotted lines in a and c represent the viability of the bacteria of stock solutions. As LSZ damages the cell walls of gram-positive bacteria *M. luteus* cells (a, b) are destroyed and the proliferation of *L. innocua* cells (c, d) is prevented.**

The effect of LSZ on the bacteria strains was observed in a control experiment using freshly prepared LSZ solutions. LSZ was added to each bacteria stock solution at concentrations of 0.05 and 0.5 mg/ml. The concentrations were chosen to resemble

the two main LSZ release pattern (Figure 5-17). Both for 0.05 and 0.5 mg/ml LSZ concentration, all *M. luteus* bacteria were killed after 24 h. For *L. innocua* the cell number decreased up to 70 % for 0.05 mg/ml LSZ and up to 92 % for 0.5 mg/ml LSZ.

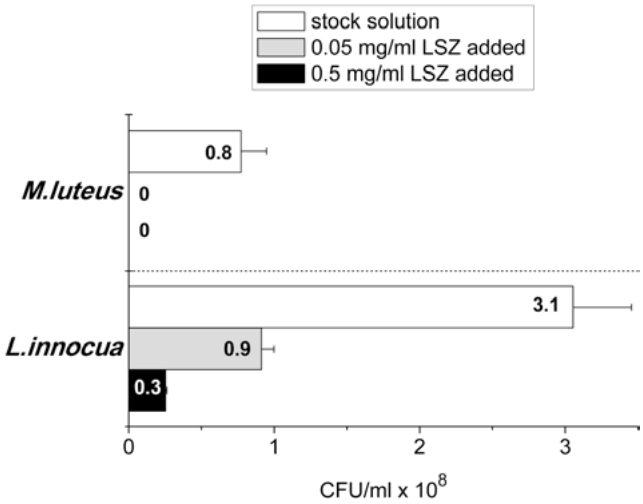


**Figure 5-17. As a control the effect of pure LSZ on the bacteria proliferation after 24 h was detected. LSZ was added to the stock solution of every bacteria strain at two different concentrations (0.05 and 0.5 mg/ml) according to the scaffolds' LSZ release. The numbers given on the bars represent total viability counts after 24 h. LSZ inhibits the proliferation of both gram-positive bacteria strains. A LSZ concentration of 0.05 mg/ml suffices to kill all *M. luteus* cells have died after 24 h. *L. innocua* shows a slightly higher resistance to LSZ. A LSZ addition of 0.5 mg/ml leads to a decrease in cell number of 92% after 24 h relative to the *L. innocua* stock solution.**

# 6 Discussion

Chapter 6.1 was adapted from:

Mueller, B.; Zacharias, M.; Rezwan, K.; Bovine Serum Albumin and Lysozyme Adsorption on Calcium Phosphate Particles. Advanced Engineering Materials, 2010, Vol. 12, I. 1-2, p. B53-61 (license number 4119441141467).

Chapter 6.2 was adapted from:

Mueller, B.; Koch, D.; Lutz, R.; Schlegel, K. A.; Treccani, L.; Rezwan, K.; A novel one-pot process for near-net-shape fabrication of open-porous resorbable hydroxyapatite/protein composites and in vivo assessment. Materials Science and Engineering: C, 2014, Vol. 42, p. 137-145 (license number 4119440246729).

Chapter 6.3 was adapted from:

Mueller, B.; Treccani, L.; Rezwan, K.; Antibacterial active open-porous hydroxyapatite/lysozyme scaffolds suitable as bone graft and depot for localised drug delivery. Journal of Biomaterials Applications, Vol. 31, I. 8, p. 1123-1134

## 6.1 Protein adsorption on calcium phosphate

Both calcium phosphate powders adsorb acidic and alkaline protein as the IEPs of the calcium phosphate powders are shifted to the IEPs of the proteins with additions of BSA and LSZ (Figure 5-2 and Figure 5-3). The change in zeta potential with increasing protein adsorption is also noticable in Figure 5-6. The fact that the IEP of the protein is reached indicates that at this stage the surface chemistry of the protein dominates over the particle's surface chemistry.

Figure 6-1 shows the measured maximum protein adsorption in relation to theoretical values for the monolayer coverage. The regular monolayer type has a jamming coverage of π/4 corresponding to 78,5% for spherical particles [120]. The values normalized on the particle surface for regular monolayer coverage were calculated from the protein molecular weight and dimension. The achievement of a regular monolayer configuration without any defects, however, is unlikely. For a more realistic assessment the random sequential adsorption model for spherical hard particles [120] was taken into account, featuring a jamming limit at 54.7%. Knowing both jamming limits, the values normalized on the particle surface for the random monolayer type were calculated from the corresponding regular monolayers shown in

Figure 5-4a and b. Electrostatic interactions are not considered for the calculation of the theoretical monolayers but play an important role under experimental conditions.

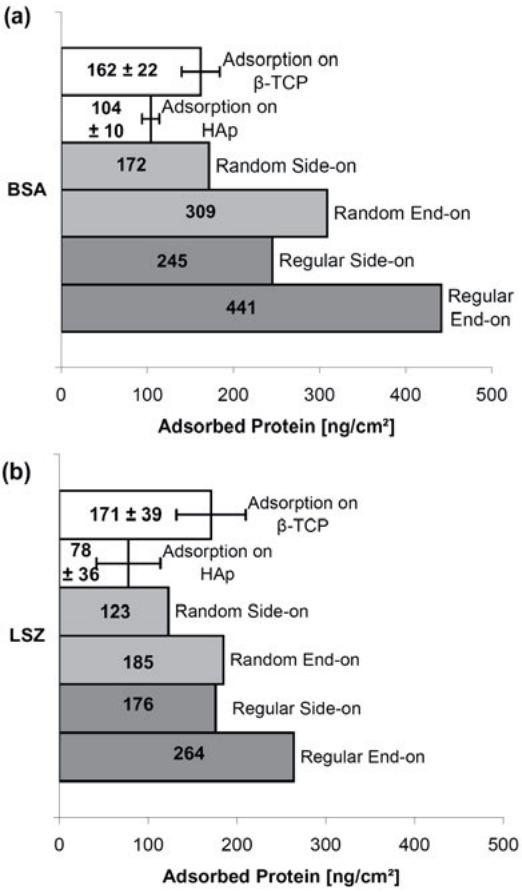


**Figure 6-1. Theoretical monolayer coverages compared to measured maximum adsorption on the calcium phosphates for BSA (a) and LSZ (b). For the regular monolayer was a jamming limit of 78.5% assumed [120]. The maximum coverages for the side-on and end-on regime normalized on the powder surface area were calculated using data from Table 4-1. For the random monolayer type the random sequential adsorption model for spherical particles [120] was assumed. The jamming limit here is 54.7% and the values normalized on the particle surface were calculated relative to the regular monolayers.**

The highest protein adsorption (at 800 ng/cm² of added protein) was detected for β-TCP and LSZ. The achieved value of 171 ± 39 ng/cm² corresponds within the error bar to the calculated regular side-on monolayer (176 ng/cm²) and the random end-on monolayer (185 ng/cm²). The BSA adsorption on β-TCP (162 ± 22 ng/cm²) fits the random side-on monolayer best (172 ng/cm²). In contrast, only semi-monolayers were roughly formed for BSA and LSZ on HAp according to the corresponding random monolayer models (Figure 6-1).

At adsorption pH, β-TCP has an initial zeta potential of -11 mV whereas HAp has a zeta potential of only -1 mV. In correlation with the measured zeta potential of the powders and the protein net charge, the protein adsorption is the highest in the case of LSZ and β-TCP where the electrostatic attraction between the positively charged protein and the negatively charged particle is the highest. LSZ and HAp are also oppositely charged but electrostatic attraction is not as strong due to the less negatively charged HAp surface. BSA and the calcium phosphate powders are both negatively charged, inducing electrostatic repulsion.

One reason for the lower protein adsorption on HAp powder might be the initially low zeta potential, implying that electrostatic interactions are weak. Another reason might be the difference in $Ca^{2+}$-solubility of the powders (Figure 5-1). The $Ca^{2+}$-solubility of HAp at adsorption pH 7 is higher as compared to β-TCP at pH 8. Hence, the surface is expected to be less stable so that adsorbed proteins can desorb easier with the continuously dissolving particle surface. In the case of HAp and LSZ (Figure 5-2b), in addition, the adsorption pH changes from 7.0 to 6.1 with increasing amount of added protein. The more acidic pH causes an even higher $Ca^{2+}$-solubility and might account for the low LSZ adsorption amount on HAp powder. This correlates well with the observed increase in conductivity at higher protein additions that can be attributed to the increasing $Ca^{2+}$-solubility and higher amounts of unbound protein.

The BSA (Figure 5-4a) and LSZ adsorption curves (Figure 5-4b) show a different development. The BSA adsorption is high at protein additions from 25 to 100 ng/cm² but hardly increases at higher initial protein concentrations. The LSZ adsorption does not stop or slow down at a certain initial protein concentration but is continuously increasing. It is probable that the maximum adsorption value for LSZ is not achieved at additions of 800 ng/cm² but the amount of adsorbed protein still increases at higher protein additions. On the contrary the maximum adsorption for BSA seems to be achieved in the experiments. Figure 5-5 reveals that an adsorption plateau between

the protein in suspension and the adsorbed protein on the surface is developing with increasing protein addition leading to a constant percentage of adsorbed protein. For BSA the adsorption plateau is reached at a protein addition of 600 ng/cm². For LSZ only half of this protein addition (200 to 400 ng/cm²) is necessary to develop an adsorption plateau. As the particle is increasingly masked with protein molecules, a charge saturation of the surface is induced and the interaction potential of the particle with subsequent protein molecules adsorbing in the process diminishes. In contrast, protein/protein interactions become more dominant. Charge saturation is reached earlier for HAp as derived from the low particle charge at adsorption pH requiring less than 75 ng/cm² of adsorbed protein to reach a constant zeta potential value whereas in the case of β-TCP more than 100 ng/cm² is required (Figure 5-6).

For LSZ protein/protein interactions seem to play a more important role as the protein adsorption is still constantly increasing after the point of charge saturation is reached. In contrast, BSA adsorption stops (for HAp) or diminishes (for β-TCP) with charge saturation (Figure 5-4). Looking at the proteins in solution this behaviour might be explained. With increasing protein concentration in aqueous media the protein molecules tend to form aggregates. For BSA a dimer formation is typical [115] whereas LSZ is known to form clusters of several molecules [122, 123]. In addition, increasing ionic strength [124, 125], as it was detected in the case of HAp and LSZ (Figure 5-2b), causes higher aggregation of LSZ molecules. Thus it is plausible that clusters of several LSZ molecules are formed on the particle surface. This might explain the continuous LSZ adsorption. On the contrary, the dimer formation of BSA might hinder the adsorption at higher BSA concentrations as the positive pole of BSA represents the favoured adsorption site for negatively charged powders and is situated closely to the dimer docking site [40].

Conformational changes due to protein adsorption may also occur [126], in particular in the case of the soft protein BSA. But they are unlikely to influence the maximum amount of adsorption. Conformational changes occur mainly at low protein surface coverage when the proteins have enough space to unfold. However, at higher protein surface coverage, protein adsorption is not restrained but protein unfolding reduces [127, 128].

Despite of the negatively charged surface of HAp and β-TCP at neutral pH both proteins, acidic and alkaline, adsorb. This is not only attributed to the fact that both proteins feature positive and negative poles but the measured zeta potential of the

particles is to be understood as a summarized net potential. This is of particular importance in the case of HAp as the zeta potential at adsorption pH is nearly zero, implicating that almost as many positive as negative adsorption sites are situated on the particle surface.

Figure 6-2 shows the calculated spatial distribution of the protein charge potentials and how they are likely orientated at the initial adsorption stage. The atomic coordinates of the proteins were taken from the protein data base [32] (pdb-entries 1HOA for BSA and 6LYZ in case of LSZ). Electrostatic potentials were calculated using the finite-difference Poisson-Boltzmann method and applying the software packages APBS and PDB2PQR [82, 83]. The charge distribution of BSA and LSZ was modelled using data files from the protein data base [32]. The red and blue colours represent equipotential surfaces with an absolute value of 30 mV. The changes in charge distribution of the proteins at the respective adsorption pHs 7 and 8 of the powders are minimal and therefore negligible. The net charge of LSZ is positive at pH 7 - 8 whereas BSA is negatively charged in this pH range. Thus it can be expected that the proteins at the first adsorption step are predominantly attracted to the negatively charged particles with domains that are positively charged. Derived from the spatial protein charge distribution side-on adsorption seems to be favoured for BSA, as most of the positive charges are located on the side of the molecule, whereas end-on adsorption is most likely for LSZ as positive charges are located at the end of the molecule (Figure 6-2). In accordance with this assumption LSZ forms an end-on monolayer on β-TCP whereas BSA forms a side-on monolayer on β-TCP (Figure 6-1) consulting the more realistic random monolayer configuration.

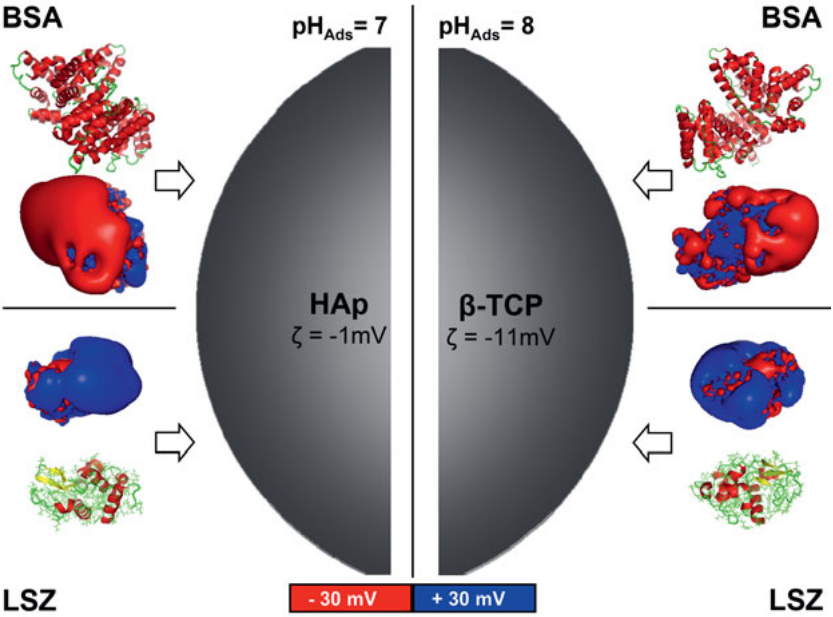


**Figure 6-2. Electrostatic potential of BSA and LSZ based on tertiary structures of the proteins using data files from the protein data bank [32] calculated for both adsorption pHs at 7 and 8. The electrostatic potentials are calculated for equipotentials of 30 mV using the finite-difference Poisson Boltzmann approach implemented in the APBS program [82]. Atomic charges were assigned using the PDB2PQR program [83]. Red areas represent negative and blue areas positive charges, respectively. Molecule orientations at the initial adsorption stage for LSZ and BSA are indicated qualitatively.**

## *6.2 Fabrication and characterisation of hydroxyapatite/protein scaffolds*

Freeze casting of ceramic slurries has been considered a highly attractive process for the fabrication of porous ceramic scaffolds for bone tissue engineering. It has gained popularity as a comparatively straightforward manufacturing route for scaffolds with controllable porosity, pore size and pore geometry [129]. Conventional freeze casting-based methods require a freeze drying step necessary to sublimate the ice formed during freezing and to avoid the destruction of the green body. In contrast,

the one-pot method presented in this study does not require any freeze drying steps due to the presence of colloidal silica. The colloidal silica particles build a strong particle network during freezing and favour the scaffold consolidation [30]. As a consequence, green bodies with a significantly higher strength than freeze-dried composites and with sufficient structural stability for handling can be obtained [96]. As no additional sintering steps are required, FG is particularly attractive to incorporate high-temperature sensitive, biorelevant molecules, such as proteins, directly to the suspension. The FG enables the incorporation of protein at high amount and no further functionalisation steps are required.

To produce crack-free composites with the one-pot freeze gelation process, a highly stabile starting suspension with good castability is fundamental. Due to the processing at pH 8 close to the isoelectric point of the HAp powder at pH 6.8, the absolute zeta potential and therefore the particle repulsion in suspension is low [114]. By adding citric acid as a dispersing agent the low zeta potential of -8 mV can be increased to -19 mV. Citric acid prevents HAp particle aggregation and improving the flow properties of the suspensions without and with proteins.

As FG does not require any sintering steps to fabricate porous green-bodies with sufficient stability, the possibility to directly incorporate proteins during scaffold processing was investigated. It was observed that protein incorporation effected composite microstructure and porosity (Figure 5-7). By conventional FG, scaffolds with interconnected porosity can be obtained as during freezing at very low temperatures generates ice channels in the composite structure, which lead to pore channel formation after drying. Scaffolds without proteins showed porosity in the nanometre range. An additional porosity could only be obtained with BSA incorporation. BSA-containing composites had an additional pore size maximum at 73.45 µm for 1 wt.% and 100.42 µm for 5 wt.% of BSA content (Table 5-2). The formation of these large pores can be related to the well-known foamability of albumin proteins [130, 131]. BSA is an amphiphilic protein with apolar and polar amino acid groups are alternating on protein surface and flexible conformation. Amphiphilic proteins possessing a high surface hydrophobicity and flexible conformation like BSA feature good emulsifying and foaming properties can strongly absorbed at the air-water interfaces and stabilise air bubbles [131-133]. Therefore it can be assumed that BSA can stabilise air bubbles formed during suspension preparation e.g. during stirring and, therefore, lead to the additional formation of micrometer-size pores. This argumentation can be applied to

explain the lack of micrometer-size pores in HAp/LSZ composites. In contrast to BSA, LSZ is a smaller globular protein with apolar amino acids concentrated in the centre and the polar amino acids on the surface and with poor foaming and emulsifying properties [131] and, therefore, unable to stabilise air bubbles. As no additional pores are generated in HAp/LSZ-5 composites their total porosity is decreased significantly as compared to protein-free composites.

The protein integration in the composites results in enhanced mechanical strength as compared to protein-free composites (Figure 5-8). The increase in strength was found to be dependent on the protein type and amount as well as on the storage conditions and the composite's total porosity. The biaxial flexure strength maxima are plotted against total porosity in Figure 5-9. A clear relationship between strength and porosity can be observed for all composite types except HAp/BSA composites. HAp/BSA-5 composites feature the highest biaxial flexure strength of all composite types despite the highest total porosity. HAp/BSA-1 composites have a higher strength comparable to that of protein-free composites, although their total porosity is considerably higher. Thus it can be reasoned that the presence of BSA which exhibits a relatively flexible structure may form a sort of network or gel-like matrix where HAp and $SiO_2$ particles are incorporated and homogenously distributed. The strength increase in HAp/LSZ composites as compared to protein-free composites can be explained by their lower porosity. Otherwise LSZ addition does not seem to have any significant positive effect on the composite strength.

To ensure reproducible testing conditions the composites were dried at controlled temperature and humidity conditions. To estimate the influence of the storage conditions on the composite strength humidity was varied. An influence of the humidity conditions during storage time on the composites' mechanical strength could most notably be observed for protein-containing composites. The HAp/BSA and HAp/LSZ composites featured a higher mechanical stability when stored at 30 % r. h. than when stored 97 % r. h. and at almost all storage times. Why 30 % r. h. lead to higher strength in the composites is not completely understood. Humidity is assumed to have a positive effect on protein networking by assisting hydrogen bonding of the proteins. How humidity might affect the cohesion abilities of the other components HAp, silica, and citric acid is not clear.

Different protein-release profiles were observed for all types of composites. The protein release was found to decreasing with increasing storage time of the composites

both at 30 % und 97 % r. h. with the exception of HAp/LSZ-5 composites stored at 97 % r. h. The decreasing protein release over storage time might be contributed to the increasing protein networking due to hydrogen bonding (see chapter 4.3). As the experiments were conducted under static conditions equilibrium between immobilised and released protein is initiated. This might be the reason for the higher percentage of protein release in composites with 5 wt.% compared to composites with 1 wt.% protein. The maximum protein release of the composites depends strongly on the type of protein used and its solubility properties. BSA as a blood protein has an exceptionally high solubility of up to 50 mg/ml whereas the solubility is of LSZ is at 15 mg/ml. If high or low protein release is desirable depends on the applied protein and its function.

Within the limits of this study, the *in vivo* results showed promising properties of the HAp/protein composites regarding initial stability, biocompatibility, resorption of the HAp material and bone regeneration in an established animal model for human bone regeneration [106].

### *6.3 Functionalisation of scaffolds with active biomolecules*

In this study it is shown that the one pot process permits the fabrication of inorganic/organic scaffolds. Firstly ice channels are generated leading to interconnected porosity. Secondly the added freeze sensitive silica sol is gelled irreversibly imparting shape stability of the scaffold. Thus sufficient mechanical strength for handling is guaranteed without any heat treatment enabling the addition of organic drugs directly to the slurry and forgoing subsequent immobilisation techniques. The slurry was stabilised with citric acid as it is, in contrast to conventional polymeric additives, non-toxic and biocompatible. Citric acid is one of the most common food additives both for flavouring and, due to its antibacterial properties, also as preservative [134, 135]. However, the applied concentration in this study is too low to have an antibacterial effect in itself so that the results of the antibacterial tests are not influenced by citric acid [136].

The porosity and strength of all fabricated scaffold types are in the range of human *Spongiosa* [57, 58, 121]. The biaxial flexure strength is increasing with increasing LSZ content with the exemption of protein-free scaffolds. When biaxial flexure strength is plotted against the scaffolds' total porosity (Figure 5-12a) it becomes apparent that the strength is dependent on porosity only and a direct influence of LSZ

on scaffold strength was not observed. In addition the lamellar, aligned micropores in scaffolds with 0.5 and 1.0 wt.% LSZ led to less stability as compared to the other scaffold types. With increasing LSZ content the porosity is decreasing leading to higher mechanical stability. The porosity of protein-free scaffolds is close to the porosity of scaffolds with 1.5 wt.% LSZ. Hence both scaffold types have comparable biaxial flexure strength. As discussed in a previous work an influence of LSZ molecules on the scaffolds' strength can be ruled out as LSZ lacks the ability for networking. This effect could up to now for the freeze gelation process only be verified for BSA and fibrinogen [137, 138] but will presumably occur for all biomolecules with networking abilities.

The porosity and structure of freeze casted scaffolds is dependent on many factors, among others particle size, solid concentration in the slurry, sample shape, and the influence of additives [139, 140]. Nanoparticles suppress the formation of aligned pores and promote the formation of numerous small pores as more nucleation sites for ice crystal growth are generated due to greater surface area [141]. As the mean particle size of the HAp powder used in this study is 100 nm it is not surprising that the formation of aligned pores is suppressed as observed in scaffolds with 0, 1.5 and 2.5 wt.% LSZ.

When LSZ is added in concentrations of 0.5 and 1.0 wt.% aligned pores are formed with pore diameters up to 100 µm. The only works currently available on the influence of protein on the structure of freeze casted scaffolds deal with gelatin (hydrolysed protein) as additive [139, 142, 143]. These works also reveal different pore morphologies and pore sizes dependant on gelatin concentration. Zhang et al. which however used a different solid content and different HAp powder particle size found up to five times larger-sized pores for scaffolds with 2 wt.% as compared to scaffolds with 6 wt.% gelatine [142].

By fabricating the scaffolds the LSZ molecules are subjected to mixing at high speed up to 2000 rpm, freezing at -150 °C, and drying for 12 weeks (Figure 4-1). The results demonstrate that the antibacterial effect of LSZ is not impaired by the processing. Moreover, the process seems to be suitable as technique for the preservation of drugs that enables and facilitates the scaffolds off-the-shelf application. Figure 5-15 shows by means of a zone-of-inhibition experimental set-up how HAp/LSZ scaffolds inhibit the growth of gram-positive *M.luteus* bacteria. The diameter of the

inhibition ring that developed around the LSZ-containing scaffolds is linearly dependent on the amount of LSZ in the scaffold.

An impact of gamma-sterilisation on LSZ activity could not be discovered. This goes along with other findings showing that gamma-sterilisation up to a dosage of 25 kGy does not or only minimally impair enzymatic activity [144, 145]. However the extent of damage by gamma-sterilisation may vary dependent on the specific biomolecule so that the applied dosage of gamma sterilization must be ascertained for the deployed drug individually [146].

A quantitative study on the antibacterial effect of LSZ on two gram-positive strains was carried out by turbidimetric measurements and total viability counts. The results of both methods are in good correlation with each other. The HAp/LSZ scaffolds had an antibacterial effect on both gram-positive bacteria strains. In the case of *M. luteus* all bacteria were destroyed. In the case of *L. innocua* an increase in bacteria number could be prevented denoting a bacteriostatic effect (Figure 5-16). For *M. luteus* a LSZ amount of 0.5 wt.% in the scaffolds corresponding to a maximum concentration of 0.04 mg/ml in the experimental setting was sufficient to destroy all bacteria after 24 h. Higher amounts of LSZ in the scaffold led to even faster dieback.

The effect of the HAp/LSZ scaffolds on gram-negative bacteria was also investigated with the bacteria strains *E. coli* and *P. fluorescens*. A bacteriostatic effect was observed up to 4 h, but after 4 h bacteria proliferation increased. This finding is not surprising as gram-negative bacteria are generally resistant to LSZ as they have thicker and more stable cell walls than gram-positive bacteria [147]. However, experiments showed that LSZ can destroy gram-negative bacteria under certain circumstances for example if modified by fatty-acid-attachment [148] or if combined with lactoferrin, another antibacterial protein [149]. In this way LSZ could be deployed against a wider range of bacteria strains.

In several studies a comparably higher biofilm formation was observed on HAp surfaces than on other ceramic surfaces as zirconia, metal surfaces as Ti or Co/Cr, and even natural surfaces as bovine bone [150-152]. Thus the appliance of antibacterial agents in connection with HAp-based bone replacement materials is highly important. The high affinity of HAp scaffolds to biofilm formation could also explain why a bacteria dieback could not be reached for *L. innocua* when in contact with HAp/LSZ scaffolds though reference experiments showed a clear antibacterial effect of LSZ on *L. innocua* (Figure 5-17).

Though LSZ has a solubility of up to 10 mg/ml the release rate was low indicating that the HAp scaffolds protected the protein from uncontrolled release. After 32 h a maximum concentration of 0.4 mg/ml was dissolved for scaffolds with 1.5 and 2.5 wt.% LSZ content. This corresponds to a release rate of 0.1 mg/h. For scaffolds with lower LSZ content, 0.5 and 1.0 wt.%, the release rate was only 0.02 mg/h. The highest percentage of LSZ released in the experimental setting after 32 h corresponded to 15 wt.% denoting that a protein content of 85 wt.% and higher remained in the scaffolds. The slope of the release curves did not decrease up to 32 h indicating ongoing release also for longer time periods (Figure 5-13). The release is regulated by initial protein content and porosity. The open porosity of the scaffolds combined with mostly nanometer-scale pore diameters secures slow drug release. The antibacterial tests showed that the low release rates were sufficient to kill bacteria. Therefore the scaffolds are a highly interesting drug delivery system that would enable constant drug supply over longer time periods at the defect site in the patient.

## *Conclusions*

The usefulness of the freeze gelation process for the fabrication of near-net-shape, open-porous calcium phosphate/protein scaffolds and their suitability as bone replacement materials regarding biocompatibility, resorbability, and drug storage and release was investigated.

The loading capacity of hydroxyapatite and β-tricalcium phosphate powders with BSA and LSZ by adsorption was studied by zeta potential and VIS spectroscopy. The added protein amount for the experiments was normalized to the surface area of the powders in the range of 25 to 800 ng/cm². Protein charge modelling gave insight into the preferred orientation of the initial protein adsorption.

A monolayer on β-TCP was reached for both proteins at 800 ng/cm². Only semi-monolayers were obtained for both proteins on HAp. The most probable reason for this finding is the lower zeta potential at the pH of adsorption of only -1mV for HAp as compared to -11mV for β-TCP. In total 162 ng/cm² of BSA and 171 ng/cm² of LSZ could be adsorbed on β-TCP. In contrast, only 104 ng/cm² of BSA and 78 ng/cm² of LSZ could be adsorbed on HAp powder. However, as the surface area of the nm-sized HAp-powder is ~40 times higher than that of the µm-sized β-TCP powder the loading capacity of the applied hydroxyapatite is non-the-less much higher than that of the applied β-TCP.

As sufficient protein adsorption on calcium phosphate in suspension was asserted HAp/protein scaffolds with 1 and 5 wt.% of protein were fabricated via a slurry route and in one step by freeze gelation process. The total porosity of the scaffolds was both for protein-free and protein-containing scaffolds in the range of spongious bone varying between 50 and 70 %. However maximum pore sizes of HAp/LSZ scaffolds were not above 33 nm. HAp/BSA scaffolds, however, featured pore sizes up to 100 µm due to the foaming effect of BSA. *Spongiosa*-like flexural strength could be reached for HAp/BSA scaffolds with 6 ± 0.4 MPa as well as for HAp/LSZ scaffolds with 5.4 ± 0.3 MPa. It was found that for both HAp/protein scaffolds the flexural strength could be considerably increased as compared to protein-free HAp scaffolds reaching only 2.9 ± 0.5 MPa. That protein incorporation into the scaffolds has a positive effect on strength was in particular ascertained by HAp/BSA scaffolds presenting the highest stability though also showing the highest porosity up to 10 % higher than protein-free

scaffolds. The strength increase of the scaffolds by protein incorporation is attributed to protein networking and an increase in elasticity.

*In vivo* experiments proofed the good biocompatibility and resorbability of the HAp/protein scaffolds with bone regeneration rates of up to 40% in 8 weeks of insertion time in the forehead region of pigs.

A further series of HAp/LSZ scaffolds with 0.5, 1, 1.5, and 2.5 was fabricated by freeze gelation process to ascertain the suitability for drug storage and release. It could be proven by bacterial tests that the antibacterial activity of LSZ was not impaired by processing. Drug release rates of 0.02 to 0.1 mg/h were ascertained which equates a release time of up to nine days. As the solubility of LSZ is relatively high with 10 mg/ml this confirms that the scaffolds protect protein from uncontrolled release and proofs the suitability of the scaffolds as drug delivery matrices. This finding most certainly originates from the nanometer-scale pores of the scaffolds.

## *Outlook*

Further studies need to investigate influences on scaffold structure and porosity in more detail. The main pore diameter of the scaffolds generated in this study was not above 50 nm. Generally pore channels with up to 20 µm in diameter are possible by freeze casting methods with water-based slurries. Higher pore diameters could be reached by using powders with µm-scale particle size instead of nano-powder. Other influences on scaffold structure are the freezing rate and direction, solvents, and additives. However non-toxic solvents and additives must be found as most works about freeze casting do not consider this aspect due to subsequent sintering. The fabricated HAp/LSZ scaffolds with LSZ amounts varying from 0.5 to 5 wt.% LSZ showed an influence on structure and pore size demonstrating that scaffold structure can also be influenced by biocompatible additives. Furthermore the foaming effect of BSA induced higher porosity which would also be an interesting topic to pursue.

Cracks in the samples were a major problem making many produced green bodies unusable. Therefore more sophisticated production methods preventing cracks by demoulding and drying could lead to higher stability. Higher strength could also be reached by networking proteins as collagen.

As the experiments were basic tests to investigate the suitability of the method further studies should concentrate on more application-oriented scaffold compositions with proteins relevant for bone modelling. These are for example collagen and bone morphogenetic proteins. In further investigations on the use of antibacterial agents antibiotics should be applied as the antibacterial effective properties of LSZ are limited to gram-positive bacteria. Finally it could be attempted to include living bone cells into scaffolds to create synthetic bone replacement materials with osteogenic properties.

# *Appendices*

## *Appendix A*

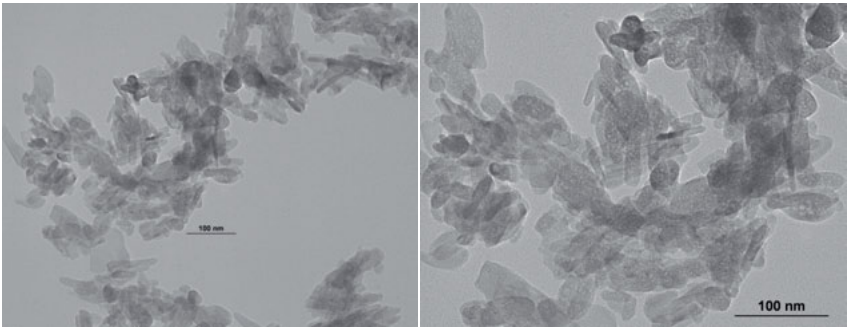


TEM pictures of hydroxyapatite powder

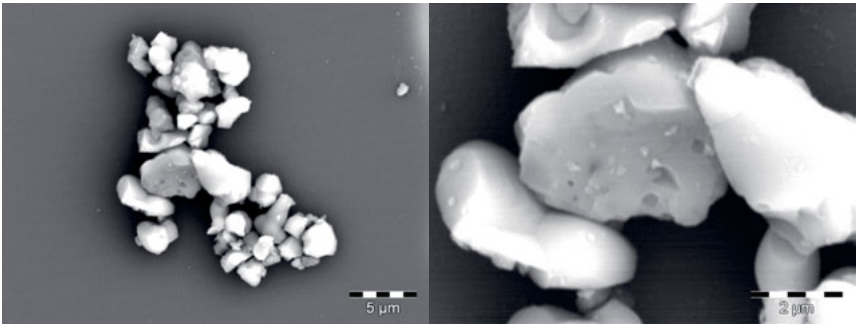


SEM pictures of β-tricalcium phosphate powder

## *Appendix B*

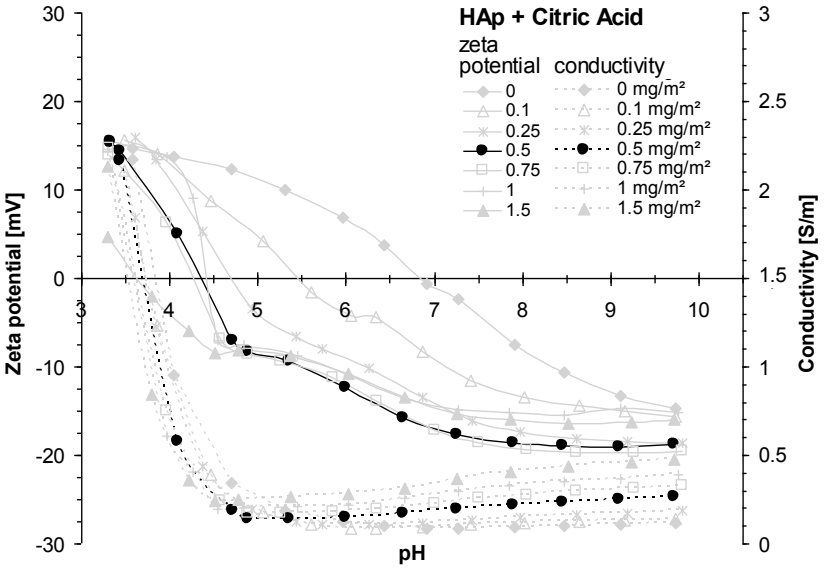


Citric acid was chosen as an efficient and non-toxic dispersing agent. The dispersing effect was demonstrated by zeta potential and conductivity measurements of 1 vol.% HAp suspensions with specific citric acid additions normalised to the HAp powder surface area. The ideal citric acid addition was found to be 0.5 mg/m² (highlighted in the diagram as a black curve). It provided the highest slurry stability due to high zeta potential and relatively low conductivity combined with good castability.

## *References*


1. Salgado, A.J., O.P. Coutinho, and R.L. Reis, *Bone tissue engineering: state of the art and future trends.* Macromol Biosci, 2004. **4**(8): p. 743-65.
2. Mandal, B.B., et al., *High-strength silk protein scaffolds for bone repair.* Proc Natl Acad Sci U S A, 2012. **109**(20): p. 7699-704.
3. Porter, J.R., T.T. Ruckh, and K.C. Popat, *Bone tissue engineering: A review in bone biomimetics and drug delivery strategies.* Biotechnology Progress, 2009. **25**(6): p. 1539-1560.
4. Bose, S., M. Roy, and A. Bandyopadhyay, *Recent advances in bone tissue engineering scaffolds.* Trends in Biotechnology, 2012. **30**(10): p. 546-554.
5. Blokhuis, T.J., *Bioresorbable bone graft substitutes*, in *Bone Substitute Biomaterials*. 2014, Woodhead Publishing. p. 80-92.
6. Blackwood, K.A., et al., *Scaffolds for growth factor delivery as applied to bone tissue engineering.* International Journal of Polymer Science, 2012.
7. Navarro, M., et al., *Biomaterials in orthopaedics.* Journal of the Royal Society Interface, 2008. **5**(27): p. 1137-1158.
8. Ji, W., et al., *Bioactive electrospun scaffolds delivering growth factors and genes for tissue engineering applications.* Pharm Res, 2011. **28**(6): p. 1259-72.
9. Simchi, A., et al., *Recent progress in inorganic and composite coatings with bactericidal capability for orthopaedic applications.* Nanomedicine-Nanotechnology Biology and Medicine, 2011. **7**(1): p. 22-39.
10. Anselmo, A.C. and S. Mitragotri, *An overview of clinical and commercial impact of drug delivery systems.* Journal of Controlled Release, 2014. **190**(0): p. 15-28.
11. Mrsny, R.J., *Oral drug delivery research in Europe.* Journal of Controlled Release, 2012. **161**(2): p. 247-253.
12. Ensign, L.M., R. Cone, and J. Hanes, *Oral drug delivery with polymeric nanoparticles: The gastrointestinal mucus barriers.* Advanced Drug Delivery Reviews, 2012. **64**(6): p. 557-570.
13. Krol, S., *Challenges in drug delivery to the brain: Nature is against us.* Journal of Controlled Release, 2012. **164**(2): p. 145-155.

14. Cima, M.J., et al., *Single compartment drug delivery.* Journal of Controlled Release, 2014. **190**(0): p. 157-171.
15. Deville, S., *Freeze-casting of porous ceramics: A review of current achievements and issues.* Advanced Engineering Materials, 2008. **10**(3): p. 155-169.
16. Scheffler, M. and P. Colombo, *Cellular ceramics*. 2004, Weinheim, Federal Republic of Germany: Wyley VCH Verlag GmbH.
17. Studart, A.R., et al., *Processing routes to macroporous ceramics: A review.* Journal of the American Ceramic Society, 2006. **89**(6): p. 1771-1789.
18. Rezwan, K., et al., *Biodegradable and bioactive porous polymer/inorganic composite scaffolds for bone tissue engineering.* Biomaterials, 2006. **27**(18): p. 3413-3431.
19. Rosa, A.L., M.r.M. Beloti, and R. van Noort, *Osteoblastic differentiation of cultured rat bone marrow cells on hydroxyapatite with different surface topography.* Dental Materials, 2003. **19**(8): p. 768-772.
20. Whitford, D., *Proteins - Structure and Function*. 2005: John Wiley & Sons, Ltd.
21. Treccani, L., et al., *Functionalized ceramics for biomedical, biotechnological and environmental applications.* Acta Biomaterialia, 2013. **9**(7): p. 7115-7150.
22. Baeza, A., I. Izquierdo-Barba, and M. Vallet-Regi, *Biotinylation of silicon-doped hydroxyapatite: a new approach to protein fixation for bone tissue regeneration.* Acta Biomater, 2010. **6**(3): p. 743-9.
23. Zurlinden, K., M. Laub, and H.P. Jennissen, *Chemical functionalization of a hydroxyapatite based bone replacement material for the immobilization of proteins.* Materialwissenschaft Und Werkstofftechnik, 2005. **36**(12): p. 820-827.
24. Hench, L.L. and J.M. Polak, *Third-generation biomedical materials.* Science, 2002. **295**(5557): p. 1014-+.
25. Böttcher, H., *Bioactive Sol-Gel Coatings.* Journal für praktische Chemie, 2000. **342**(5): p. 427-436.
26. Carturan, G., et al., *Inorganic gels for immobilization of biocatalysts: inclusion of invertase-active whole cells of yeast (saccharomyces cerevisiae) into thin layers of SiO2 gel deposited on glass sheets.* Journal of Molecular Catalysis, 1989. **57**(1): p. L13-L16.

27. Jacques, L. and et al., *Encapsulation of biomolecules in silica gels.* Journal of Physics: Condensed Matter, 2001. **13**(33): p. R673.
28. Koch, D., et al., *Evolution of Porosity by Freeze Casting and Sintering of Sol-Gel derived Ceramics.* J. Sol-Gel Sci. Tech. , 2003. **26**(1-3): p. 149-152.
29. Soltmann, U., et al., *Freeze gelation: A new option for the production of biological ceramic composites (Biocers).* Materials Letters, 2003. **57**(19): p. 2861-2865.
30. Pulkin, M., D. Koch, and G. Grathwohl, *Silica Effect on Porous Calcium Phosphate Ceramics from the Freeze Gelation Route.* Int. J. Appl. Ceram. Techol., 2010 - in print(1-11).
31. Kolk, A., et al., *Current trends and future perspectives of bone substitute materials - From space holders to innovative biomaterials.* Journal of Cranio-Maxillofacial Surgery, 2012. **40**(8): p. 706-718.
32. *RCSB Protein data base*, http://www.rcsb.org (accessed July 2008).
33. Carter, D.C. and J.X. Ho, *Structure of Serum-Albumin*, in *Advances in Protein Chemistry, Vol 45*. 1994, Academic Press Inc: San Diego. p. 153-203.
34. Sugio, S., et al., *Crystal structure of human serum albumin at 2.5 angstrom resolution.* Protein Engineering, 1999. **12**(6): p. 439-446.
35. Diamond, R., *Real-space refinement of the structure of hen egg-white lysozyme.* J Mol Biol, 1974. **82**(3): p. 371-91.
36. Rezwan, K., et al., *Change of xi potential of biocompatible colloidal oxide particles upon adsorption of bovine serum albumin and lysozyme.* Journal of Physical Chemistry B, 2005. **109**(30): p. 14469-14474.
37. Krajewski, A., A. Piancastelli, and R. Malavolti, *Albumin adhesion on ceramics and correlation with their Z-potential.* Biomaterials, 1998. **19**(7-9): p. 637-641.
38. Norde, W. and A.C.I. Anusiem, *Adsorption, Desorption and Readsorption of Proteins on Solid-Surfaces.* Colloids and Surfaces, 1992. **66**(1): p. 73-80.
39. Rezwan, K., L.P. Meier, and L.J. Gauckler, *A prediction method for the isoelectric point of binary protein mixtures of bovine serum albumin and lysozyme adsorbed on colloidal Titania and alumina particles.* Langmuir, 2005. **21**(8): p. 3493-3497.
40. Rezwan, K., et al., *Bovine serum albumin adsorption onto colloidal Al2O3 particles: A new model based on zeta potential and UV-vis measurements.* Langmuir, 2004. **20**(23): p. 10055-10061.

41. Adamczyk, Z., *Particle adsorption and deposition: role of electrostatic interactions.* Advances in Colloid and Interface Science, 2003. **100-102**: p. 267-347.
42. Jönsson, B. and J. Ståhlberg, *The electrostatic interaction between a charged sphere and an oppositely charged planar surface and its application to protein adsorption.* Colloids and Surfaces B: Biointerfaces, 1999. **14**(1-4): p. 67-75.
43. Roth, C.M., J.E. Sader, and A.M. Lenhoff, *Electrostatic Contribution to the Energy and Entropy of Protein Adsorption.* Journal of Colloid and Interface Science, 1998. **203**(1): p. 218-221.
44. Ravichandran, S. and J. Talbot, *Mobility of adsorbed proteins: A Brownian dynamics study.* Biophysical Journal, 2000. **78**(1): p. 110-120.
45. Claesson, P.M., et al., *Protein interactions at solid surfaces.* Advances in Colloid and Interface Science, 1995. **57**: p. 161-227.
46. Wahlgren, M. and T. Arnebrant, *Protein Adsorption to Solid-Surfaces.* Trends in Biotechnology, 1991. **9**(6): p. 201-208.
47. McKenzie, H.A. and F.H. White Jr, *Lysozyme and α-Lactalbumin: Structure, Function, and Interrelationships*, in *Advances in Protein Chemistry*. 1991, Academic Press. p. 173-315.
48. Yang, V.C., J.F. Liang, and Y.T. Li, *Biomedical application of immobilized enzymes.* Journal of Pharmaceutical Sciences, 2000. **89**(8): p. 979-990.
49. Kim, J., J.W. Grate, and P. Wang, *Nanostructures for enzyme stabilization.* Chemical Engineering Science, 2006. **61**(3): p. 1017-1026.
50. Olszta, M.J., et al., *Bone structure and formation: A new perspective.* Materials Science & Engineering R-Reports, 2007. **58**(3-5): p. 77-116.
51. Jackson, S.A., A.G. Cartwright, and D. Lewis, *The morphology of bone mineral crystals.* Calcified Tissue Research, 1978. **25**(1): p. 217-222.
52. Wopenka, B. and J.D. Pasteris, *A mineralogical perspective on the apatite in bone.* Materials Science and Engineering: C, 2005. **25**(2): p. 131-143.
53. Buehler, M.J., *Nature designs tough collagen: Explaining the nanostructure of collagen fibrils.* PNAS, 2006. **103**(33): p. 12285-12290.
54. Orgel, J.P.R.O., et al., *Microfibrillar structure of type I collagen in situ.* PNAS, 2006. **103**(24): p. 9001-9005.
55. Gupta, H.S., et al., *Cooperative deformation of mineral and collagen in bone at the nanoscale.* PNAS, 2006. **0604237103**.

56. Blair, H.C., *How the osteoclast degrades bone.* Bioessays, 1998. **20**(10): p. 837-46.
57. Stone, J.L., G.S. Beaupre, and W.C. Hayes, *Multiaxial strength characteristics of trabecular bone.* Journal of Biomechanics, 1983. **16**(9): p. 743-752.
58. Hench, L., *Bioceramics: From Concept to Clinic.* J. Am. Ceram. Soc., 1991. **74**: p. 1487-1510.
59. LeGeros, R.Z., *Properties of osteoconductive biomaterials: Calcium phosphates.* Clinical Orthopaedics and Related Research, 2002(395): p. 81-98.
60. Salgado, A.J., O.P. Coutinho, and R.L. Reis, *Bone Tissue Engineering: State of the Art and Future Trends.* Macromolecular Bioscience, 2004. **4**(8): p. 743-765.
61. Burg, K.J.L., S. Porter, and J.F. Kellam, *Biomaterial developments for bone tissue engineering.* Biomaterials, 2000. **21**(23): p. 2347-2359.
62. Bauer, T.W. and G.F. Muschler, *Bone graft materials - An overview of the basic science.* Clinical Orthopaedics and Related Research, 2000(371): p. 10-27.
63. Zimmermann, G. and A. Moghaddam, *Allograft bone matrix versus synthetic bone graft substitutes.* Injury, 2011. **42, Supplement 2**: p. S16-S21.
64. Bohner, M., *Resorbable biomaterials as bone graft substitutes.* Materials Today, 2010. **13**(1-2): p. 24-30.
65. Lemons, J.E., F. Misch-Dietsh, and M.S. McCracken, *Chapter 4 - Biomaterials for Dental Implants*, in *Dental Implant Prosthetics (Second Edition)*. 2015, Mosby: St. Louis. p. 66-94.
66. Nair, L.S. and C.T. Laurencin, *Biodegradable polymers as biomaterials.* Progress in Polymer Science, 2007. **32**(8-9): p. 762-798.
67. Huang, J. and S. Best, *1 - Ceramic biomaterials for tissue engineering*, in *Tissue Engineering Using Ceramics and Polymers (Second Edition)*. 2014, Woodhead Publishing. p. 3-34.
68. Chevalier, J., et al., *Critical effect of cubic phase on aging in 3 mol% yttria-stabilized zirconia ceramics for hip replacement prosthesis.* Biomaterials, 2004. **25**(24): p. 5539-5545.
69. Kokubo, T., *Bioactive glass ceramics: properties and applications.* Biomaterials, 1991. **12**(2): p. 155-163.

70. Gallea, S., et al., *Activation of mitogen-activated protein kinase cascades is involved in regulation of bone morphogenetic protein-2-induced osteoblast differentiation in pluripotent C2C12 cells.* Bone, 2001. **28**(5): p. 491-498.
71. Yeaman, M.R. and N.Y. Yount, *Mechanisms of Antimicrobial Peptide Action and Resistance.* Pharmacological Reviews, 2003. **55**(1): p. 27-55.
72. Dorozhkin, S., *Calcium orthophosphates.* Journal of Materials Science, 2007. **42**(4): p. 1061-1095.
73. Ferraz, M.P., F.J. Monteiro, and C.M. Manuel, *Hydroxyapatite nanoparticles: A review of preparation methodologies.* Journal of Applied Biomaterials & Biomechanics, 2004. **2**(4): p. 74.
74. Cüneyt Tas, A., *Synthesis of biomimetic Ca-hydroxyapatite powders at 37°C in synthetic body fluids.* Biomaterials, 2000. **21**(14): p. 1429-1438.
75. Nolze, G., *PowderCell 2.3*, Bundesanstalt für Materialforschung und -prüfung: Berlin.
76. Hughes, J.M., M. Cameron, and K.D. Crowley, *Structural variations in natural F, OH, and Cl apatites.* American Mineralogist, 1989. **74**: p. 870-876.
77. Destainville, A., et al., *Synthesis, characterization and thermal behavior of apatitic tricalcium phosphate.* Materials Chemistry and Physics, 2003. **80**(1): p. 269-277.
78. Yashima, M., et al., *Crystal structure analysis of Beta-tricalcium phosphate Ca3(PO4)2 by neutron powder diffraction.* Journal of Solid State Chemistry, 2003. **175**(2): p. 272-277.
79. Stryer, L., *Biochemistry - Fifth edition*. 2002: W. H. Freeman and Company.
80. Sakou, T., *Bone Morphogenetic Proteins: From Basic Studies to Clinical Approaches.* Bone, 1998. **22**(6): p. 591-603.
81. Carter, D.C., et al., *Three-dimensional structure of human serum albumin.* Science, 1989. **244**(4909): p. 1195-1198.
82. Baker, N.A., et al., *Electrostatics of nanosystems: Application to microtubules and the ribosome.* Proceedings of the National Academy of Sciences of the United States of America, 2001. **98**(18): p. 10037-10041.
83. Dolinsky, T.J., et al., *PDB2PQR: an automated pipeline for the setup of Poisson-Boltzmann electrostatics calculations.* Nucleic Acids Research, 2004. **32**: p. W665-W667.

84. Burton, W.G., et al., *Separation of proteins by reversed-phase high-performance liquid chromatography : I. Optimizing the column.* Journal of Chromatography A, 1988. **443**: p. 363-379.
85. Salmang, H. and H. Scholze, *Keramik*. 2007, Berlin, Heidelberg: Springer Verlag.
86. Rezwan, K., *Protein treated aqueous Colloidal Oxide Particle Suspensions: Driving Forces for Protein Adsorption and Conformational Changes*. 2005, ETH Zurich: Zurich.
87. Dukhin, A.S. and P.J. Goetz, *Ultrasound for characterizing colloids. Particle sizing, zeta potential and rheology.* 2002: Elsevier.
88. O'Brien, R.W., *Electro-acoustic effects in a dilute suspension of spherical particles.* Journal of Fluid Mechanics, 1988. **190**: p. 71-86.
89. Kollenberg, W., ed. *Technische Keramik*. 2004, Vulkan-Verlag GmbH: Essen, Deutschland.
90. Weast, R.C., ed. *Handbook of chemistry and physics*. 57th ed. 1976, CRC Press, Inc: Cleveland, Ohio.
91. Schüth, F., K.S.W. Sing, and J. Weitkamp, eds. *Handbook of porous solids*. 2002, WYLEY-VHC Verlag GmbH: Weinheim, Federal Republic of Germany.
92. Schwartzwalder, K. and A.V. Somers, *Method of making porous ceramic articles*, in *United States Patent Office*, G.M. Corporation, Editor. 1963: United States of America.
93. Gonzenbach, U.T., et al., *Ultrastable particle-stabilized foams.* Angewandte Chemie-International Edition, 2006. **45**(21): p. 3526-3530.
94. Barg, S., et al., *New cellular ceramics from high alkane phase emulsified suspensions (HAPES).* Journal of the European Ceramic Society, 2009. **29**(12): p. 2439-2446.
95. Deville, S., et al., *Freezing as a path to build complex composites.* Science, 2006. **311**(5760): p. 515-518.
96. Soltmann, U., et al., *Freeze gelation: A new option for the production of biological ceramic composites (Biocers).* Materials Letters, 2003. **57**(19): p. 2861-2865.
97. Borger, A., P. Supancic, and R. Danzer, *The ball on three balls test for strength testing of brittle discs: stress distribution in the disc.* Journal of the European Ceramic Society, 2002. **22**(9-10): p. 1425-1436.

98. Shetty, D.K., et al., *Biaxial Flexure Tests for Ceramics.* American Ceramic Society Bulletin, 1980. **59**(12): p. 1193-1197.
99. Ren, F., et al., *Resonant ultrasound spectroscopy measurement of Young's modulus, shear modulus and Poisson's ratio as a function of porosity for alumina and hydroxyapatite.* Philosophical Magazine, 2009. **89**(14): p. 1163-1182.
100. Maes, K.J. and J.M. Willems, *Photochemistry: UV/VIS Spectroscopy, Photochemical Reactions and Photosynthesis*. 2011: Nova Science Publishers.
101. Bradford, M.M., *A rapid and sensitive method for the quantitation of microgram quantities of protein utilizing the principle of protein-dye binding.* Analytical Biochemistry, 1976. **72**(1-2): p. 248-254.
102. Gitelman, H.J., *An improved automated procedure for the determination of calcium in biological specimens.* Analytical Biochemistry, 1967. **18**(3): p. 521-531.
103. McFarland, J., *The nephelometer: An instrument for estimating the number of bacteria in suspensions used for calculating the opsonic index and for vaccines.* Journal of the American Medical Association, 1907. **XLIX**(14): p. 1176-1178.
104. Roessler, W.G. and C.R. Brewer, *Permanent Turbidity-Standards.* Applied and environmental microbiology, 1967. **15**(5): p. 1114-1121.
105. Lutz, R., et al., *Bone regeneration after topical BMP-2-gene delivery in circumferential peri-implant bone defects.* Clin Oral Implants Res, 2008. **19**(6): p. 590-9.
106. Schlegel, K.A., et al., *Preclinical animal model for de novo bone formation in human maxillary sinus.* Oral Surg Oral Med Oral Pathol Oral Radiol Endod, 2009. **108**(3): p. e37-44.
107. Tudor, C., et al., *Static and dynamic periosteal elevation: a pilot study in a pig model.* International journal of oral and maxillofacial surgery, 2010. **39**(9): p. 897-903.
108. Lutz, R., et al., *Biofunctionalization of titanium implants with a biomimetic active peptide (P-15) promotes early osseointegration.* Clin Oral Implants Res, 2010. **21**(7): p. 726-34.

109. Postgate, J.R. and J.R.N.a.D.W. Ribbons, *Chapter XVIII Viable counts and Viability*, in *Methods in Microbiology*. 1969, Academic Press. p. 611-628.
110. Bauer, A.W., D.M. Perry, and W.M. Kirby, *Single-disk antibiotic-sensitivity testing of staphylococci: An analysis of technique and results.* A.M.A. Archives of Internal Medicine, 1959. **104**(2): p. 208-216.
111. Pan, X.Y., et al., *Self-assembly of beta-casein and lysozyme.* Journal of Colloid and Interface Science, 2007. **316**(2): p. 405-412.
112. Dismer, F. and J. Hubbuch, *A novel approach to characterize the binding orientation of lysozyme on ion-exchange resins.* Journal of Chromatography A, 2007. **1149**(2): p. 312-320.
113. Blindow, S., et al., *Hydroxylapatite / SiO2 composites via freeze casting for bone tissue engineering.* Advanced Engineering Materials (Cover Page), 2009. **11**(11): p. 875-884.
114. Mueller, B., M. Zacharias, and K. Rezwan, *Bovine Serum Albumin and Lysozyme Adsorption on Calcium Phosphate Particles.* Advanced Engineering Materials (Inside Cover Page), 2010. **12**(1-2): p. B53-61.
115. Jachimska, B., M. Wasilewska, and Z. Adamczyk, *Characterization of Globular Protein Solutions by Dynamic Light Scattering, Electrophoretic Mobility, and Viscosity Measurements.* Langmuir, 2008. **24**(13): p. 6866-6872.
116. Lethaus, B., et al., *Guided bone regeneration: Dynamic procedures versus static shielding in an animal model.* Journal of Biomedical Materials Research Part B: Applied Biomaterials, 2010. **95B**(1): p. 126-130.
117. Bauer, A.W., D.M. Perry, and W.M.M. Kirby, *Single disc antibiotic sensitivity testing of Staphylococci.* AMA Arch Intern Med, 1959. **104**: p. 208-216.
118. *Sterilization of health care products - Radiation - Part 2: Establishing the sterilization dose*. 2013: ISO 11137-2.
119. Lide, D.R., *Handbook of Chemistry and Physics* 1994: CRC Press, Inc.
120. Adamczyk, Z., *Particles at interfaces, Interactions, Deposition, Structure*. 2006: Elsevier.
121. Kaplan, S.J., et al., *Tensile strength of bovine trabecular bone.* Journal of Biomechanics, 1985. **18**(9): p. 723-727.
122. Stradner, A., et al., *Equilibrium cluster formation in concentrated protein solutions and colloids.* Nature, 2004. **432**(7016): p. 492-495.

123. Kim, D.T., H.W. Blanch, and C.J. Radke, *Direct imaging of lysozyme adsorption onto mica by atomic force microscopy.* Langmuir, 2002. **18**(15): p. 5841-5850.
124. Cardinaux, F., et al., *Modeling equilibrium clusters in lysozyme solutions.* Epl, 2007. **77**(4): p. -.
125. Sear, R.P., *Interactions in protein solutions.* Current Opinion in Colloid & Interface Science, 2006. **11**(1): p. 35-39.
126. Shen, J.-W., et al., *Molecular simulation of protein adsorption and desorption on hydroxyapatite surfaces.* Biomaterials, 2008. **29**(5): p. 513-532.
127. Serro, A.P., et al., *Bovine serum albumin conformational changes upon adsorption on titania and on hydroxyapatite and their relation with biomineralization.* Journal of Biomedical Materials Research Part A, 2004. **70A**(3): p. 420-427.
128. Brandes, N., et al., *Adsorption-induced conformational changes of proteins onto ceramic particles: Differential scanning calorimetry and FTIR analysis.* Journal of Colloid and Interface Science, 2006. **299**(1): p. 56-69.
129. Wegst, U.G., et al., *Biomaterials by freeze casting.* Philos Transact A Math Phys Eng Sci, 2010. **368**(1917): p. 2099-121.
130. Mleko, S., et al., *Rheological properties of foams generated from egg albumin after pH treatment.* Lwt-Food Science and Technology, 2007. **40**(5): p. 908-914.
131. Kato, A., et al., *Functional properties of cross-linked lysozyme and serum albumin.* Journal of Agricultural and Food Chemistry, 1986. **34**(2): p. 370-372.
132. Garrn, I., et al., *Clot-forming: the use of proteins as binders for producing ceramic foams.* Journal of the European Ceramic Society, 2004. **24**(3): p. 579-587.
133. Helenius, A. and K. Simons, *Charge shift electrophoresis: simple method for distinguishing between amphiphilic and hydrophilic proteins in detergent solution.* Proceedings of the National Academy of Sciences, 1977. **74**(2): p. 529-532.
134. Mishra, S.K., A. Shrivastav, and S. Mishra, *Effect of preservatives for food grade C-PC from Spirulina platensis.* Process Biochemistry, 2008. **43**(4): p. 339-345.

135. Delwiche, J., *The impact of perceptual interactions on perceived flavor.* Food Quality and Preference, 2004. **15**(2): p. 137-146.
136. Firouzabadi, F.B., et al., *ZnO nanoparticle suspensions containing citric acid as antimicrobial to control Listeria monocytogenes, Escherichia coli, Staphylococcus aureus and Bacillus cereus in mango juice.* Food Control, 2014. **42**(0): p. 310-314.
137. Hess, U., et al., *A mild one-pot process for synthesising hydroxyapatite/biomolecule bone scaffolds for sustained and controlled antibiotic release.* Biomedical Materials, 2015. **10**(1): p. 015013.
138. Mueller, B., et al., *A novel one-pot process for near-net-shape fabrication of open-porous resorbable hydroxyapatite/protein composites and in vivo assessment.* Materials Science and Engineering: C, 2014. **42**(0): p. 137-145.
139. Li, W.L., K. Lu, and J.Y. Walz, *Freeze Casting of Porous Materials: Review of Critical Factors in Microstructure Evolution.* International materials reviews, 2012. **57**(1): p. 37-58.
140. Deville, S., E. Saiz, and A.P. Tomsia, *Freeze casting of hydroxyapatite scaffolds for bone tissue engineering.* Biomaterials, 2006. **27**(32): p. 5480-5489.
141. McKee, C.T. and J.Y. Walz, *Effects of Added Clay on the Properties of Freeze-Casted Composites of Silica Nanoparticles.* Journal of the American Ceramic Society, 2009. **92**(4): p. 916-921.
142. Zhang, Y., K. Zuo, and Y.-P. Zeng, *Effects of gelatin addition on the microstructure of freeze-cast porous hydroxyapatite ceramics.* Ceramics International, 2009. **35**(6): p. 2151-2154.
143. Swain, S.K. and D. Sarkar, *Preparation of nanohydroxyapatite gelatin porous scaffold and mechanical properties at cryogenic environment.* Materials Letters, 2013. **92**(0): p. 252-254.
144. Furuta, M., M. Oka, and T. Hayashi, *Radiation sterilization of enzyme hybrids with biodegradable polymers.* Radiation Physics and Chemistry, 2002. **63**(6): p. 323-325.
145. Zulli, G., et al., *Influence of gamma radiation onto polymeric matrix with papain.* Radiation Physics and Chemistry, 2010. **79**(3): p. 286-288.
146. Ijiri, S., et al., *Effect of sterilization on bone morphogenetic protein.* Journal of orthopaedic research, 1994. **12**(5): p. 628-36.

147. Benkerroum, N., *Antimicrobial activity of lysozyme with special relevance to milk.* African Journal of Biotechnology, 2008. **7**(25): p. 4856-4867.
148. Ibrahim, H.R., K. Kobayashi, and A. Kato, *Length of Hydrocarbon Chain and Antimicrobial Action to Gram-Negative Bacteria of Fatty Acylated Lysozyme.* Journal of Agricultural and Food Chemistry, 1993. **41**(7): p. 1164-1168.
149. Ellison, R.T. and T.J. Giehl, *Killing of Gram-Negative Bacteria by Lactoferrin and Lysozyme.* Journal of Clinical Investigation, 1991. **88**(4): p. 1080-1091.
150. Guerreiro-Tanomaru, J.M., et al., *Comparative Analysis of Enterococcus faecalis Biofilm Formation on Different Substrates.* Journal of Endodontics, 2013. **39**(3): p. 346-350.
151. Ichikawa, et al., *In vitro adherence of Streptococcus constellatus to dense hydroxyapatite and titanium.* Journal of Oral Rehabilitation, 1998. **25**(2): p. 125-127.
152. Li, J., et al., *Biofilm formation of Candida albicans on implant overdenture materials and its removal.* Journal of Dentistry, 2012. **40**(8): p. 686-692.

## *Author's publications*

(1) Mueller, B.; Zacharias, M.; Rezwan, K.
Bovine Serum Albumin and Lysozyme Adsorption on Calcium Phosphate Particles
*Advanced Engineering Materials*, 2010 (Vol. 12, I. 1-2, p. B53-61)

(2) Mueller, B.; Koch, D.; Lutz, R.; Schlegel, K. A.; Treccani, L.; Rezwan, K.
A novel one-pot process for near-net-shape fabrication of open-porous resorbable hydroxyapatite/protein composites and in vivo assessment
*Materials Science and Engineering: C*, 2014 (Vol. 42, p. 137-145)

(3) Mueller, B.; Treccani, L.; Rezwan, K.
Antibacterial active open-porous hydroxyapatite/lysozyme scaffolds suitable as bone graft and depot for localised drug delivery
*Journal of Biomaterials Applications, Vol. 31, I. 8, p. 1123-1134*

# Online-Buchshop für Ingenieure

**VDI nachrichten** **BUCHSHOP**

Online-Shops

**Fachliteratur und mehr - jetzt bequem online recherchieren & bestellen unter: www.vdi-nachrichten.com/Der-Shop-im-Ueberblick**


**Täglich aktualisiert: Neuerscheinungen VDI-Schriftenreihen**


Im Buchshop von vdi-nachrichten.com finden Ingenieure und Techniker ein speziell auf sie zugeschnittenes, umfassendes Literaturangebot.

Mit der komfortablen Schnellsuche werden Sie in den VDI-Schriftenreihen und im Verzeichnis lieferbarer Bücher unter 1.000.000 Titeln garantiert fündig.

Im Buchshop stehen für Sie bereit:

**VDI-Berichte** und die Reihe **Kunststofftechnik:**

Berichte nationaler und internationaler technischer Fachtagungen der VDI-Fachgliederungen

**Fortschritt-Berichte VDI:**

Dissertationen, Habilitationen und Forschungsberichte aus sämtlichen ingenieurwissenschaftlichen Fachrichtungen

**Newsletter „Neuerscheinungen":**

Kostenfreie Infos zu aktuellen Titeln der VDI-Schriftenreihen bequem per E-Mail

**Autoren-Service:**

Umfassende Betreuung bei der Veröffentlichung Ihrer Arbeit in der Reihe Fortschritt-Berichte VDI

**Buch- und Medien-Service:**

Beschaffung aller am Markt verfügbaren Zeitschriften, Zeitungen, Fortsetzungsreihen, Handbücher, Technische Regelwerke, elektronische Medien und vieles mehr – einzeln oder im Abo und mit weltweitem Lieferservice

## Die Reihen der Fortschritt-Berichte VDI:

1 Konstruktionstechnik/Maschinenelemente
2 Fertigungstechnik
3 Verfahrenstechnik
4 Bauingenieurwesen
5 Grund- und Werkstoffe/Kunststoffe
6 Energietechnik
7 Strömungstechnik
8 Mess-, Steuerungs- und Regelungstechnik
9 Elektronik/Mikro- und Nanotechnik
10 Informatik/Kommunikation
11 Schwingungstechnik
12 Verkehrstechnik/Fahrzeugtechnik
13 Fördertechnik/Logistik
14 Landtechnik/Lebensmitteltechnik
15 Umwelttechnik
16 Technik und Wirtschaft
17 Biotechnik/Medizintechnik
18 Mechanik/Bruchmechanik
19 Wärmetechnik/Kältetechnik
20 Rechnerunterstützte Verfahren (CAD, CAM, CAE CAQ, CIM ...)
21 Elektrotechnik
22 Mensch-Maschine-Systeme
23 Technische Gebäudeausrüstung

ISBN 978-3-18-329417-6